

Fluid Evolution of the Monte Mattoni Mafic Complex, Adamello Batholith, Northern Italy: Insights from Fluid Inclusion Analysis and Thermodynamic Modeling

Journal Article

Author(s):

Hennings, Sibylle K; Wagner, Thomas; [Ulmer, Peter](#) ; [Heinrich, Christoph A.](#) 

Publication date:

2017-08

Permanent link:

<https://doi.org/10.3929/ethz-b-000278249>

Rights / license:

[In Copyright - Non-Commercial Use Permitted](#)

Originally published in:

Journal of Petrology 58(8), <https://doi.org/10.1093/petrology/egx068>

Fluid Evolution of the Monte Mattoni Mafic Complex, Adamello Batholith, Northern Italy: Insights from Fluid Inclusion Analysis and Thermodynamic Modeling

Sibylle K. Hennings¹, Thomas Wagner^{2*}, Peter Ulmer¹ and Christoph A. Heinrich¹

¹Institute for Geochemistry and Petrology, ETH Zurich, Clausiusstr. 25, CH-8092 Zurich, Switzerland; ²Applied Mineralogy and Economic Geology, RWTH Aachen University, Wüllnerstrasse 2, 52062 Aachen, Germany

*Corresponding author. E-mail: thomas.wagner@iml.rwth-aachen.de

Received September 20, 2016; Accepted October 11, 2017

ABSTRACT

The magmatic–hydrothermal fluid evolution in the Monte Mattoni mafic complex in the Adamello batholith was reconstructed based on a combination of fluid inclusion studies (microthermometry and laser ablation inductively coupled plasma mass spectrometry microanalysis of individual fluid inclusions) and thermodynamic modeling of subsolidus fluid–mineral equilibria. The mafic complex consists of two main units, the Monte Mattoni and the Cadino gabbros, both of which show textural evidence for fluid saturation. In the Mattoni gabbro, which is crowded with equant amphibole phenocrysts forming local cumulate layers, fluid saturation was probably reached as a result of rapid magma ascent and pressure decrease. Some of the exsolved fluid phase was trapped in ocelli (miarolitic cavities of subcentimeter size) occurring in the matrix of the porphyritic gabbro. The overlying and locally transgressive Cadino gabbro consists of needle-shaped amphibole grains that crystallized together with plagioclase at the emplacement level of laterally extensive sills. The Cadino magma reached fluid saturation after progressive crystallization as shown by miarolitic cavities that formed in the center of local pegmatitic pods. Five distinct fluid inclusion types (A to E) are present as texturally and compositionally consistent assemblages in a clear relative chronology. The earlier fluid inclusion types, A to C, are three-phase aqueous–carbonic and show a decrease in salinity (from 7.9 to 5.5 wt % equivalent NaCl), coupled with a decrease in CO₂ concentration, with time. The salinity in later two-phase aqueous fluid inclusion types D and E increases again (to 9.5 and 27.1 wt % equivalent NaCl), whereas the CO₂ concentration drops to very low values. The Ca/Na ratio in the aqueous fluids increases and the late-stage type E fluids are concentrated calcic–sodic brines. The initial decrease in salinity and CO₂ content can be explained by fluid–melt partitioning during successive stages of fluid exsolution from the magma at a minimum pressure of 150 MPa. The reversal to increasing salinity in late-stage aqueous fluids is the consequence of water-consuming subsolidus reactions of the fluid with the surrounding rocks, forming epidote, chlorite and calcite at low fluid/rock ratios. The subsolidus evolution is quantified by fluid–mineral equilibria modeling, which predicts the observed mineral transformations, the systematic variation in chemical composition of the fluids, and the decrease in their CO₂ concentration as a result of calcite precipitation. Isochores constructed for the five inclusion types indicate an approximate pressure–temperature path starting with isobaric cooling for the early aqueous–carbonic fluid inclusion types at 250 MPa, followed by a substantial pressure decrease during the entrapment of increasingly saline aqueous inclusions. The late-stage calcic brine inclusions were entrapped at temperatures as low as 250°C, where brittle fracturing marks the transition to near-hydrostatic fluid

pressure. The ore metal contents (Cu, Pb, Zn, W, Pb and Mn) and the S content of aqueous–carbonic fluid inclusions in the Monte Mattoni complex are comparatively low, in comparison with typically more differentiated intrusions associated with porphyry copper deposits worldwide. Low concentrations in ore-forming components, even in this mafic magma, indicate a weak endowment with ore-forming components already determined in the mantle source of the Adamello magmas. This lack of fertility for ore formation may be explained by restricted subduction metasomatism in an orogen dominated by collision and slab break-off.

Key words: magmatic–hydrothermal; fluid inclusions; LA-ICP-MS; thermodynamic modeling; Adamello batholith

INTRODUCTION

The evolution of magmatic–hydrothermal fluids is intimately linked to the evolution of ascending and crystallizing magmas. Hydrous calc-alkaline magmas contain substantial amounts of dissolved volatiles, with their solubility being controlled by the bulk composition of the melt and the pressure–temperature (P – T) conditions of the magmatic system (Holtz *et al.*, 1995, 2001; Clemens & Watkins, 2001). When volatile solubility is exceeded in response to decreasing P during magma ascent or crystallization of less hydrous minerals owing to heat loss during emplacement in the crust, a magmatic–hydrothermal fluid will exsolve from the magma (Burnham, 1967; Burnham & Ohmoto, 1980; Hedenquist & Lowenstern, 1994; Candela, 1997; Webster, 2004). This fluid can be either a single phase of liquid- to vapor-like density (loosely called a ‘super-critical fluid’), or coexisting liquid and vapor phases (Shinohara, 1994; Dolejs, 2007; Liebscher & Heinrich, 2007).

The processes controlling fluid exsolution from crystallizing magmas play a central role in the formation of magmatic–hydrothermal systems and related ore deposits. Granitoid rocks are an important source of economically important metals such as Cu, Mo, Sn, W and Au (Kesler & Simon, 2015), but the factors that govern the mineralization potential of granitoid intrusions are not yet fully understood. Of particular importance is the question of whether fundamental differences exist between the composition (concentrations of ore metals and complexing ligands) of magmatic–hydrothermal fluids in barren and mineralized intrusions and whether these relate to the melt source or to magma evolution during ascent. Several geochemical criteria including major element composition (Mason & Feiss, 1979; Lang & Titley, 1998), mineral chemistry (Kesler *et al.*, 1975; Hendry *et al.*, 1985), and isotope signatures (Farmer & DePaolo, 1984; Lang & Titley, 1998) have been utilized to distinguish productive from barren intrusions. Attempts to relate magma fertility for ore formation to the tectonic setting of magma generation and lower-crustal mixing and fractionation are extensive (Rohrlach & Loucks, 2005; Sillitoe, 2010; Richards, 2011; Lu *et al.*, 2015). Early fluid inclusion and petrological–geochemical studies in several porphyry copper ore

deposits have linked fluid evolution with the crystallization and subsolidus history of their host intrusions (Roedder, 1971; Eastoe, 1978; Reynolds & Beane, 1985).

Recent fluid inclusion studies based on laser ablation inductively coupled plasma mass spectrometry (LA-ICP-MS) microanalysis of individual inclusions have focused on comparing the metal inventory of mineralized and barren intrusions. The fluid inclusion study of two barren porphyry systems (Audétat & Pettke, 2003) demonstrated that the absolute metal concentrations and the salinity in the fluids appear to be low compared with mineralized systems. It was concluded that less efficient metal extraction from the melt was a key factor that prevented substantial ore metal enrichment. Audétat *et al.* (2008) summarized and compared fluid inclusion compositions in several barren and mineralized systems. As a general conclusion, most primary magmatic–hydrothermal fluids are initially single-phase and of low salinity; their metal concentrations correlate positively between the type and metal budget of ore mineralization and the composition of the associated intrusion. Fluids in barren systems are comparatively metal poor. These observations are consistent with the results of a fluid inclusion study by Bodnar (1995), who concluded that in porphyry copper systems early fluids exsolving from the magma contain the highest concentrations of ore metals. The overall picture that emerges from these studies is that early magmatic processes, from the source of magmas in metasomatized mantle (Richards, 2011) through to the injection of mafic magmas into more felsic upper crustal magma reservoirs (Halter *et al.*, 2005), contribute decisive steps on the way towards eventual formation of hydrothermal vein networks and the rare culmination in large economic ore deposits.

In this study, we report the results of a comprehensive fluid inclusion study using state-of-the-art LA-ICP-MS analysis of individual fluid inclusions in amphibole gabbros of the Monte Mattoni mafic complex, southern Adamello batholith (northern Italy). This complex is a particularly interesting natural laboratory because: (1) miarolitic cavities that host well-preserved fluid inclusion assemblages are abundant, in contrast to more felsic plutons in the same batholith; (2) the host-rocks are essentially gabbroic in composition and thus record the

fluid evolution in previously under-studied primitive magmas at an early stage of igneous differentiation.

THE ADAMELLO BATHOLITH

The Adamello batholith is a triangle-shaped intrusive complex in the Southern Alps, located in the Italian regions of Lombardy in the west and Trentino and Alto Adige in the east. It is exposed over an area of c. 670 km², elongated in a SW–NE direction, has a maximum length of around 80 km and a vertical extent of up to 3 km (Bianchi *et al.*, 1970; Blundy & Sparks, 1992; Schoene *et al.*, 2012; Broderick *et al.*, 2015). The northern and eastern margins of the Adamello are confined by two intersecting Alpine lineaments, the Periadriatic Tonale Line and the Giudicaria Line offsetting it (Fig. 1). The Adamello is a composite batholith consisting of 12 major granitoid plutons and numerous smaller mafic intrusions (Bianchi *et al.*, 1970). It is the largest of a group of Tertiary calc-alkaline intrusions that intruded during the later stages of the Alpine orogeny. These are referred to as ‘Periadriatic intrusions’, because they followed collision of the Adriatic microcontinent with Europe, probably subsequent to slab break-off after limited subduction (von Blanckenburg & Davies, 1995). All Periadriatic plutons (e.g. Biella, Bergell, Rieserferner, Reschen) show a close spatial association with the Periadriatic fault system, which facilitated the ascent and emplacement of magma (Laubscher, 1983; Schoene *et al.*, 2012).

The Adamello batholith intrudes schists and gneisses of the southern Alpine crystalline basement and its unmetamorphosed Permo-Triassic sedimentary cover rocks, which were subjected to high-grade contact metamorphism and metasomatism (Brack, 1981; Gieré, 1990; Gieré & Williams, 1992; Gerdes *et al.*, 1995). The magma emplacement was sequential, with the oldest plutons in the south (42 Ma) and the youngest in the north (29 Ma) (Del Moro *et al.*, 1983b; Blundy & Sparks, 1992; Schaltegger *et al.*, 2009; Schoene *et al.*, 2012; Broderick *et al.*, 2015). This long-lived emplacement history is also reflected in SW–NE gradients in chemical and isotopic composition, notably a systematic increase in whole-rock ⁸⁷Sr/⁸⁶Sr and δ¹⁸O values from south to north (Cortecci *et al.*, 1979; Del Moro *et al.*, 1983a). The continuous variation in major and certain trace elements suggests an assimilation–fractional crystallization (AFC) process from a mafic parental magma that evolved towards a granodioritic magma through segregation of clinopyroxene and amphibole (Macera *et al.*, 1983).

This study concentrates on the gabbros of the Monte Mattoni mafic complex (Fig. 1) in the southern part of the Adamello batholith (Bianchi *et al.*, 1970). The southern part of the Adamello batholith is characterized by partly isolated bodies of ultramafic to gabbroic igneous rocks that accompany the tonalitic–trondhjemitic granitoids, with which they have a common magmatic origin. The main processes responsible for the differentiation

of the mafic–ultramafic magmatic rocks are fractional crystallization with minor assimilation in the underlying crust and upper mantle (Ulmer *et al.*, 1985).

PETROLOGY OF THE STRATIFIED MONTE MATTONI MAFIC COMPLEX

Monte Mattoni exposes a small mafic intrusive body over an elevation of c. 2000–2200 m south of Monte Cadino and Monte Frerone in the Val Fredda complex (Fig. 1b). The intrusion has a complex internal structure composed of several magmatic pulses, which were emplaced sill-like to form distinct, subhorizontal layers of different types of gabbro within a predominantly felsic plutonic unit (tonalite to granodiorite; Blundy & Sparks, 1992). The magmatic layers have thicknesses of a few decimeters to tens of meters, most distinctly developed at Monte Mattoni and the adjacent Monte Cadino (Fig. 1b). Some outcrops show discordant intrusive relationships recording successive pulses of emplacement of distinct magma types (Fig. 2). In the following description of field and textural relations, we have adopted and further defined the lithological terms introduced in the first petrographic study by Sonderegger (1980).

Mattoni gabbro and hornblendite

The medium- to coarse-grained Mattoni gabbro occupies the lower parts of the small mountain and attains up to 50 m vertical extent near a small pass SW of the peak (Fig. 1b). It has a porphyritic texture of euhedral, short prismatic to equant, black hornblende phenocrysts up to 1 cm in size set in a fine-grained slightly greenish matrix composed of strongly zoned plagioclase, hornblende and clinopyroxene (Fig. 3). The overall texture is cumulitic, indicating settling of early formed hornblende, grading to almost pure hornblendite cumulates. The hornblende phenocrysts show macroscopically visible zoning, with sharp contacts between core and rim. This is mainly due to abundant inclusions of granular and strongly corroded olivine, clinopyroxene and minor orthopyroxene and spinel in the core of the hornblende phenocrysts, resulting in a poikilitic appearance. The cores also show more pronounced alteration than the rims, locally with an even later overgrowth of greenish actinolite. The plagioclase within the matrix is coarse grained, interstitial (inter-cumulus) and shows extensive zoning ranging from An₉₀ cores to An₁₀ rims, consistent with equilibrium crystallization of the intercumulus melt. Clinopyroxene grains are small compared with the plagioclase, but have euhedral crystal shapes and pronounced Fe–Mg core–rim zoning as well as sector zoning (high- and low-Al sectors). Occasionally, some interstitial quartz and/or calcite is observed. The granular and corroded clinopyroxene within the hornblendes of the Mattoni gabbro and the associated hornblendite have an Mg-rich augitic composition with a relatively low Al content

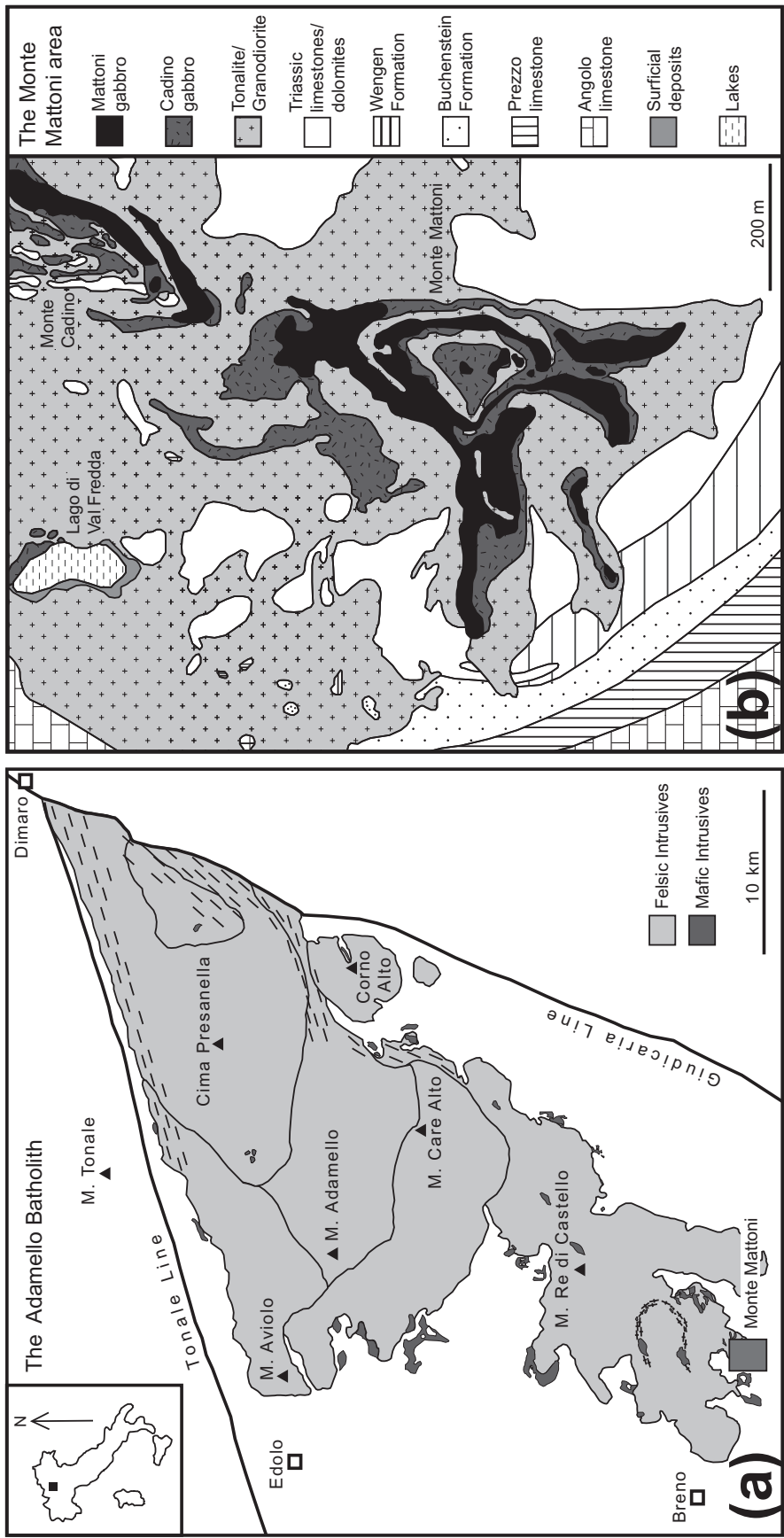


Fig. 1. Geological maps of (a) the Adamello batholith in the Central Alps and (b) the Monte Mattoni mafic complex, which is located in the south of the Re di Castello Pluton. Redrawn and modified after Bianchi *et al.* (1970), Blundy & Sparks (1992) and P. Brack (unpublished data).

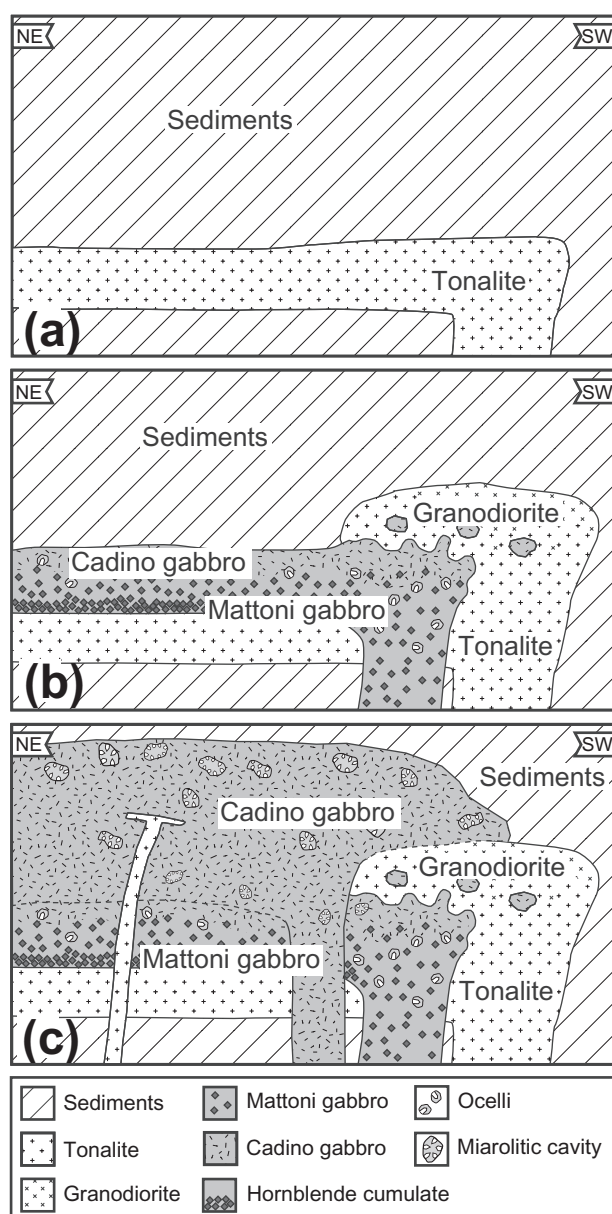


Fig. 2. Schematic field relations between petrographically distinct types of ultramafic to intermediate igneous lithologies at Monte Mattoni, indicating the likely sequence of emplacement and local differentiation of different magma types [based on Blundy & Sparks (1992) and authors' own observations]. The sequence encompasses (a) early tonalite and granodiorite intrusion, followed by (b) porphyritic Mattoni gabbro depositing hornblende cumulates and locally mingling with still partly liquid tonalite–granodiorite magma, and finally (c) emplacement and local crystallization of the Cadino gabbro, which fractionated *in situ* through to residual pegmatites that eventually exsolved magmatic–hydrothermal fluid to form crystal-lined miarolitic cavities. Although outcrop exposure is insufficient for complete mapping, the interpreted final geometry in (c) schematically approximates a NE–SW section through the northwestern flank of Monte Mattoni, with the main feeder dikes most probably located beneath the small ridge west of Monte Mattoni or in the poorly exposed cirque to its north (Fig. 1b).

(4 wt %), whereas the clinopyroxene in the gabbro matrix is augite with variable, but generally higher Al content (up to 8 wt %) and lower Mg content. These differences in mineral chemistry suggest that the

hornblende phenocrysts did not crystallize in equilibrium with their matrix at the conditions of emplacement, but are inherited from a deeper magma reservoir (Ulmer *et al.*, 1985).

The Mattoni gabbro contains round ocelli (Fig. 4a); that is, small miarolitic cavities of sub-centimeter size (0.2–0.8 cm), which are bordered by narrow green clinopyroxene rims that are present as palisades. The central parts of the ocelli commonly contain euhedral grains of quartz. The remaining space is completely filled with K-feldspar and/or calcite. Angus (1962) first described this feature as ocellar, and interpreted it as an amygdaloidal texture; that is, representing former fluid bubbles filled with secondary minerals. The highest abundance of ocelli (about 5 vol. %) occurs at the small mountain pass west of Monte Mattoni where the Mattoni gabbro also exhibits the thickest exposure and locally shows steep contacts against tonalite, consistent with proximity to an inferred feeder structure in this area (Fig. 2).

Especially in its upper parts, the Mattoni gabbro shows *in situ* differentiation of the matrix and local fractionation towards more felsic rocks. The gabbro becomes progressively finer grained, the modal proportion of large hornblende phenocrysts decreases, and the abundance of ocelli increases significantly. In the center of these more differentiated zones, segregated pockets of restitic melt are found, which are surrounded by a sharp border towards the gabbro (Fig. 3). The pockets are enriched in coarser grained igneous plagioclase and quartz, locally exhibiting graphic intergrowth, and the sharp front delimits patchy development of minor secondary epidote, chlorite and hornblende in the surrounding host-rock. Locally, this differentiation leads to the formation of open miarolitic cavities lined with euhedral crystals of quartz and plagioclase. The surroundings of these fluid pockets are vuggy with millimeter-sized cavities resembling merging ocelli. Quartz crystals up to 2 cm in the miarolitic cavities are milky owing to the presence of abundant fluid inclusions; the plagioclase shows oscillatory zoning and pronounced sericitization. South of Monte Mattoni, a phenocryst-poor variant of the Mattoni gabbro occurs as enclaves in tonalite, which implies that both magmas were emplaced in short succession. The upper contact of the Mattoni gabbro is poorly defined and possibly gradual or interlayered with the Cadino gabbro.

Cadino gabbro

The Cadino gabbro occupies most of the upper 100 m of Monte Mattoni and appears lighter colored than the Mattoni gabbro. On the lower west flank of the hill, steep dike contacts show that the Cadino gabbro intruded into existing cumulate layers of the Mattoni gabbro (Fig. 2), but higher up the contact is poorly defined and possibly gradational. Hornblende grains in the Cadino gabbro have a distinctly elongate prismatic to acicular shape and are intergrown with plagioclase

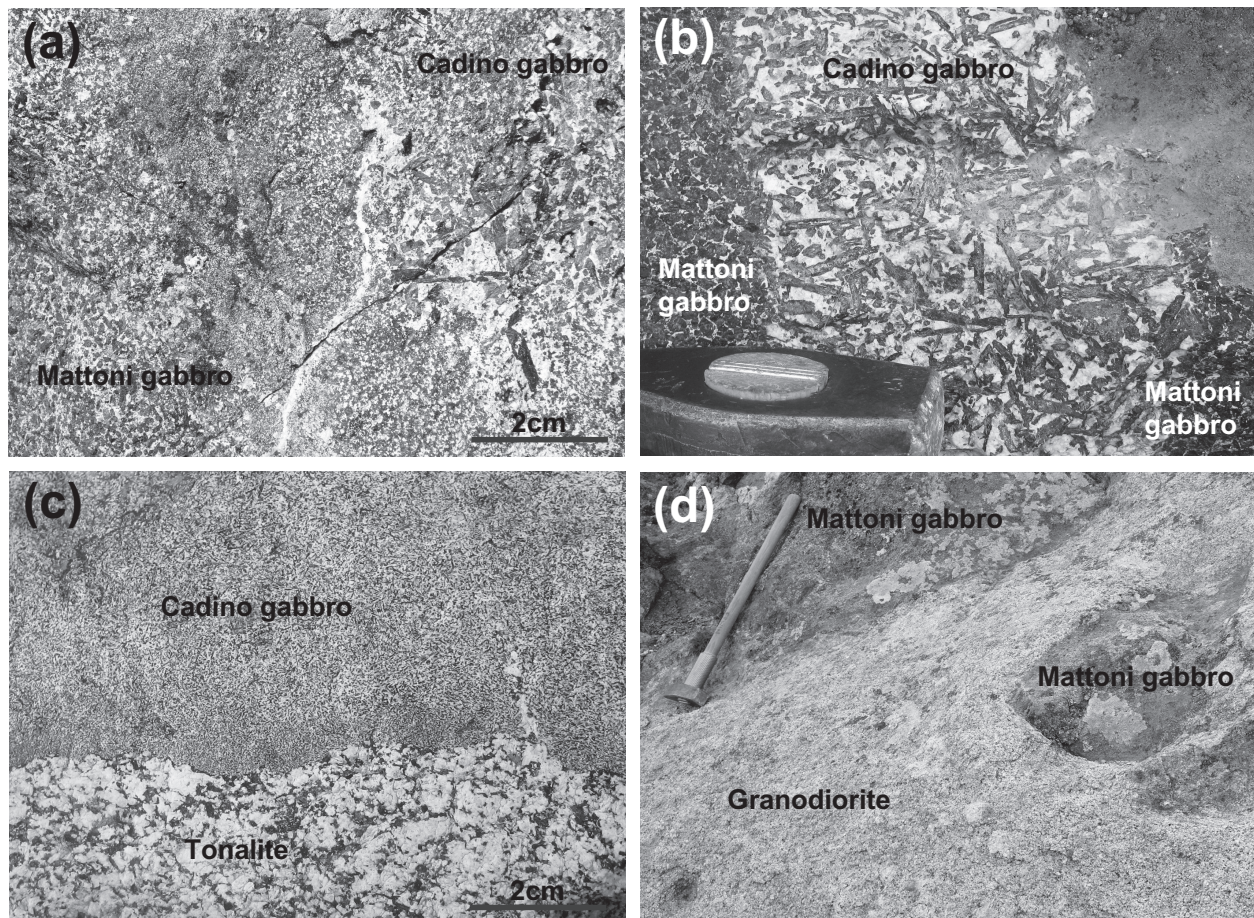


Fig. 3. Field relationships in the Monte Mattoni mafic complex. (a) Gradual transition between the Mattoni gabbro and the Cadino gabbro. (b) Dike of Cadino gabbro crosscutting the Mattoni gabbro. (c) Contact of tonalite–granodiorite with the Cadino gabbro. The gabbro shows a chilled margin; small dikes of mobilized tonalite were injected into contraction cracks in the rapidly cooled gabbro. (d) Mafic enclaves of Mattoni gabbro inside tonalite–granodiorite.

and minor quartz. In some places, the hornblende crystals have a shorter prismatic shape resulting in an equigranular textural appearance (possibly transitional to the matrix material of the Mattoni gabbro; Figs 2b and 3d). The plagioclase has an anhedral shape with continuous zoning from anorthite-rich cores to andesine rims (Blundy & Shimizu, 1991). The euhedral hornblende crystals have brown cores and green rims, and contain small inclusions of plagioclase. The Cadino gabbro is texturally heterogeneous, with the grain size of the hornblende crystals varying gradually from a few millimeters to several centimeters in length and around 1 cm in thickness. Pegmatitic pods up to 30 cm in size contain coarse hornblende with skeletal shapes, K-feldspar and major quartz, in addition to plagioclase. Commonly, the pegmatitic pods become coarser and lighter inwards, towards local miarolitic cavities measuring up to 10 cm in size (Fig. 4c and d). The abundance and size of the miarolitic cavities increase towards the top of Monte Mattoni. Mineralogically, they show clear zoning from the pegmatitic margin towards the open center. The marginal zone is composed of subhedral quartz, plagioclase and minor epidote, followed by a zone with euhedral quartz crystals that grow towards

the center. The central vug is partly filled by epidote and chlorite associated with the euhedral quartz crystals (Fig. 5). The same hydrous silicates form limited and commonly sharply bounded alteration patches in the surrounding gabbro, out to a few tens of centimeters from the miarolitic cavities (Fig. 4).

Tonalite and porphyritic granodiorite

The tonalite is a leucocratic equigranular to weakly porphyritic rock that is composed of plagioclase, quartz, biotite and hornblende. The porphyritic granodiorite is also leucocratic and has the same mineralogy as the tonalite, but quartz and plagioclase appear as phenocrysts and the rock contains less mafic minerals and minor interstitial K-feldspar. In the field, gradual transitions between the two rock types are commonly observed and they have been classified as a single unit. Tonalite and porphyritic granodiorite are found intermingled with both the Mattoni and Cadino gabbros. The Monte Mattoni gabbros, however, occur only in the cores of the mafic sheets and are, without exception, separated from the felsic rocks by variable thickness selvages of Cadino gabbro (Blundy & Sparks, 1992).

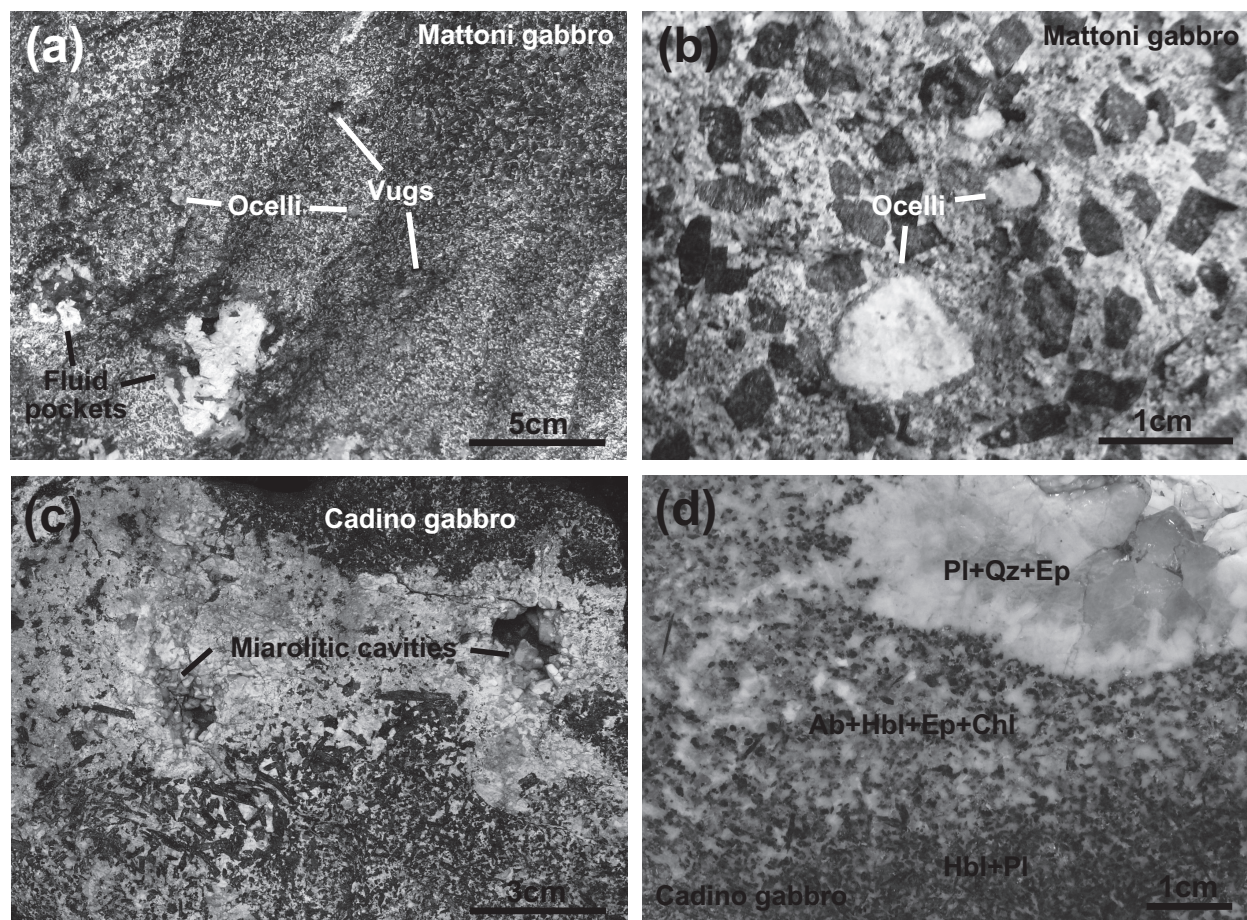


Fig. 4. Textures showing fluid saturation in the Monte Mattoni mafic complex. (a) Local differentiation in the Mattoni gabbro, which results in the segregation of fluid pockets filled with minerals crystallized from a water-saturating residual melt. The abundance of ocelli and vugs surrounding the pockets, as well as the decrease in grain size, should be noted. (b) Ocelli in the Mattoni gabbro. The narrow clinopyroxene rim and the euhedral shape of the quartz crystals should be noted. (c) Miarolitic cavities forming in the center of pegmatitic pods. (d) Detail of a miarolitic cavity in the Cadino gabbro containing a free-standing quartz crystal overgrowing albitic feldspar + quartz + minor epidote in a graphic intergrowth. In the lighter-colored halo around the pocket, amphibole is partly altered to epidote + chlorite, compared with the dark fresh gabbro at the bottom of the photograph (sample SHA-0709–42).

Mafic enclaves of gabbro are commonly present within the tonalite–granodiorite (Fig. 3d). In several places, the Cadino gabbro shows a chilled margin at the contact with the tonalite–granodiorite. In addition, the tonalite–granodiorite shows apophyses that penetrate into the Cadino gabbro (Figs 2 and 3c). Notably, no evidence of fluid separation has been observed in the felsic rocks.

Evidence for fluid saturation

The mafic rocks at Monte Mattoni show two distinct features recording two different styles of fluid saturation: the ocelli and pegmatitic pockets of residual volatile-rich melt (Fig. 5). The ocelli demonstrate most probably the first exsolving fluid batches, in response to rapid magma rise and *P* decrease; that is, first boiling in the sense of Burnham (1967). The differentiation of the gabbro into pockets of segregated residual melt demonstrates the local accumulation of residual and probably H₂O-rich melt. Eventually, these pockets exsolved a separate magmatic–hydrothermal fluid phase by second boiling (Burnham, 1967), forming the miarolitic cavities.

Both the ocelli and the residual melt pockets are therefore formed in an environment of incipient fluid saturation, but by different mechanisms that are likely to be reflected by fluids of different composition, as shown in the following section.

FLUID INCLUSION STUDY

The fluid inclusion study focused on fluids trapped in ocelli from the Mattoni gabbro and miarolitic cavities from the Cadino gabbro. Twenty-three samples displaying features indicative of fluid saturation were collected in the field and were examined microscopically. Based on reconnaissance petrography, four representative samples containing fluid inclusion assemblages with well-defined textural and temporal relationships were selected for microthermometry. Finally, two samples containing fluid inclusion assemblages with sufficiently large inclusions (30–50 μm) were analyzed for their elemental composition by LA-ICP-MS (Table 1).

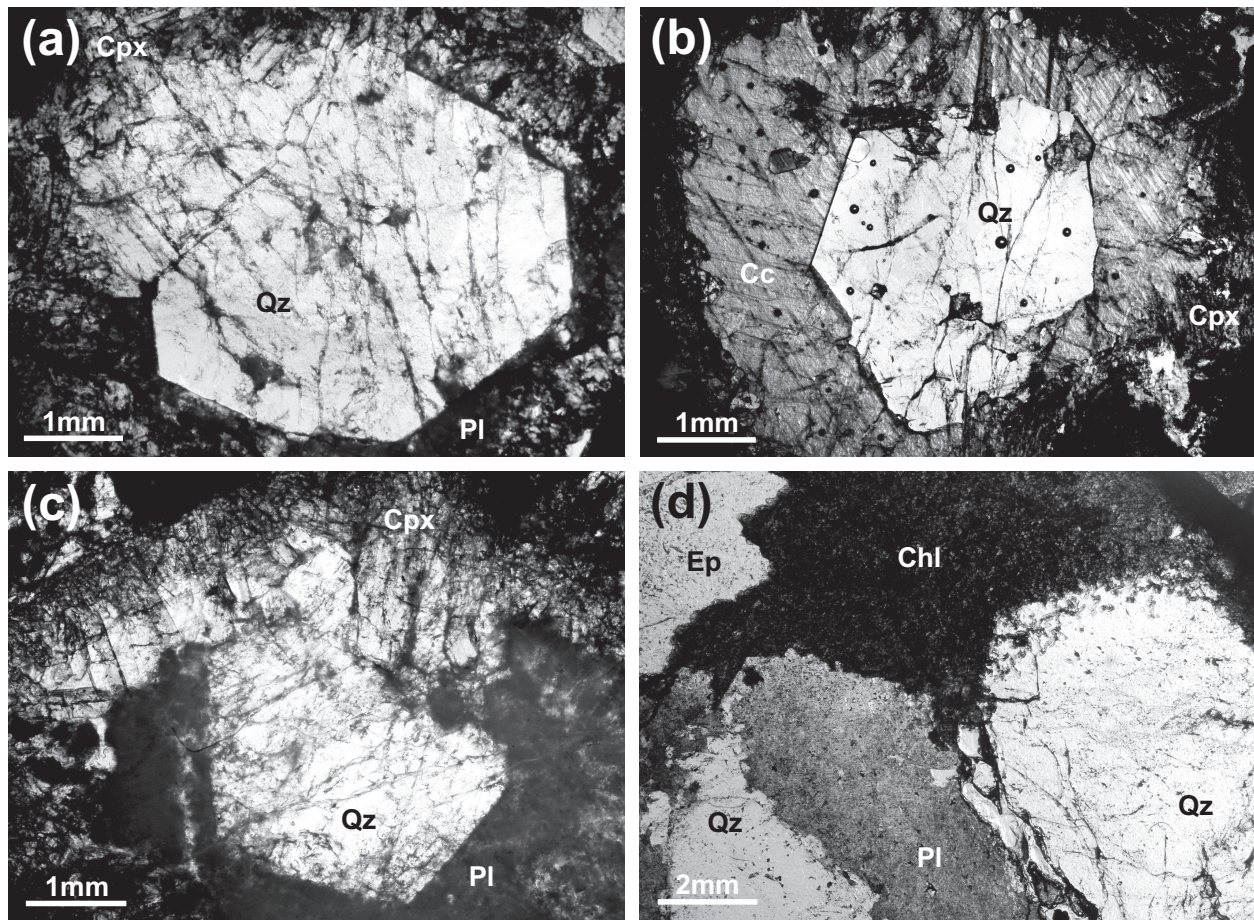


Fig. 5. Photomicrographs illustrating fluid saturation features in the Monte Mattoni mafic complex. (a) Ocellus filled by quartz (Qz), inside plagioclase (Pl) + clinopyroxene (Cpx). (b) Ocellus, filled by euhedral quartz and late calcite (Cc). (c) Ocellus with a marginal rim of clinopyroxene and a center filled with quartz and plagioclase. (d) Section through a miarolitic cavity, with the mineral sequence epidote (Ep) followed by chlorite (Chl) + euhedral quartz.

Table 1: Average phase transition temperatures determined from microthermometry and corresponding calculated bulk fluid properties for each fluid inclusion assemblage (FIA) investigated

Sample type	FI type	FIA	<i>n</i>	<i>T</i> _{mCO₂} (°C)	<i>T</i> _{mice} (°C)	<i>T</i> _{mclath} (°C)	<i>T</i> _{hCO₂} (°C)	<i>T</i> _{htotal} (°C)	Salinity (wt %)	Density (g cm ⁻³)	<i>X</i> _{CO₂}
<i>Sample SHA-0608-6</i>											
Ocelli (Mattoni gabbro)	A	A1	1				29.7				
	A	A2	2				29.1 (0.5)				
	A	A3	4				28.7 (0.1)				
	A	A4	4				29.0 (1.4)				
<i>Sample SHA-0709-37</i>											
Fluid pocket (Mattoni gabbro)	A	A5	6	-56.9 (0.2)		5.9 (0.2)	29.3 (0.2)		7.5 (0.0)	0.91	0.137
	A	A6	6			5.7 (0.1)	29.8 (0.5)		7.8 (0.1)	0.91	0.137
	A	A7	2	-56.8		5.4 (0.0)	30.3 (0.2)		8.3 (0.0)	0.91	0.137
<i>Sample SHA-0709-42</i>											
Miarolitic cavity (Cadino gabbro)	B	B1	13	-56.6 (0.1)		7.1 (0.1)	30.9 (0.1)	334 (10)	5.5 (0.3)	0.90	0.106
	C	C1	7	-56.8 (0.2)		8.2 (0.2)	31.0 (0.1)	310 (3)	3.7 (0.2)	0.79	0.057
	C	C2	10	-56.6 (0.1)		8.2 (0.2)	31.0 (0.1)	310 (4)	3.5 (0.5)	0.79	0.057
	D	D1	12	-57.1 (0.1)	-6.4 (0.9)			360 (6)	9.7 (1.2)	0.72	
	D	D2	11	-57.1 (0.1)	-6.9 (0.1)	9.2 (0.1)		350 (8)	9.1 (3.3)	0.74	
	D	D3	15	-57.1 (0.1)	-5.7 (0.4)	9.1 (0.4)		351 (13)	8.8 (0.6)	0.72	
<i>Sample SHA-0709-44</i>											
Miarolitic cavity (Cadino gabbro)	E	E1	9		-26.9 (0.2)				26.7 (0.1)		
	E	E2	8		-27.1 (0.2)				26.9 (0.1)		
	E	E3	11		-28.3 (2.0)			179	27.6 (1.2)	1.11	

Numbers in parenthesis are 1σ standard deviations. *n*, number of fluid inclusions measured for each FIA. Partial homogenization of CO₂ in aqueous-carbonic fluid inclusions occurred into the liquid phase (LLV → LL) in type A and type B inclusions, and into the vapor phase (LLV → LV) in type C inclusions.

Analytical techniques

Microthermometric measurements were performed on doubly polished sections (200–400 μm thickness) using an Olympus petrographic microscope equipped with a Linkam THMSG-600 cooling–heating stage. For three-phase aqueous–carbonic fluid inclusions the following phase transition temperatures were measured: final melting temperature of CO_2 ($T_{m\text{CO}_2}$), ice ($T_{m\text{ice}}$) and clathrate ($T_{m\text{clath}}$), homogenization temperature of CO_2 liquid and gas (Th_{CO_2}), and total homogenization of the CO_2 phase with the aqueous solution (Th_{total}). For two-phase aqueous fluid inclusions only $T_{m\text{ice}}$ and Th_{total} were measured. The freezing temperatures of ice and CO_2 and the initial ice melting temperature were also recorded. All measurements were performed twice with a heating rate of $0.1^\circ\text{C min}^{-1}$ close to the phase transitions, except for the total homogenization temperature, which was measured with a heating rate of 1°C min^{-1} . Calibration was done on synthetic fluid inclusion standards (SYNFLINC) using the triple points of CO_2 (-56.6°C) and H_2O (0.0°C), and the critical point of pure H_2O (374.1°C). Reproducibility of melting and CO_2 homogenization temperatures is of the order of $\pm 0.1^\circ\text{C}$, and reproducibility of total homogenization temperatures is around $\pm 1^\circ\text{C}$. Apparent salinities are reported in weight per cent equivalent (eqv.) NaCl, based on final melting of ice (Bodnar & Vityk, 1994) or CO_2 clathrate (Diamond, 1992). All measurements up to the temperature of CO_2 homogenization were done prior to LA-ICP-MS measurements. The total homogenization temperature was measured after LA-ICP-MS analysis using the remaining fluid inclusions of the same assemblages, to avoid decrepitation or leaking.

For all aqueous (H_2O –NaCl) fluid inclusions, the bulk density was calculated from the microthermometric data. This was done for fluid inclusions with salinities up to 10 wt % eqv. NaCl (type A, B, C and D inclusions) using the empirical model for phase equilibria in the H_2O –NaCl system (Driesner & Heinrich, 2007; Driesner, 2007). The density of aqueous fluid inclusions with higher salinity (type E inclusions) was calculated with the program AqSoVir (Bakker, 2003) using the equation of state of Oakes *et al.* (1990). The density of aqueous–carbonic (H_2O – CO_2 –NaCl) fluid inclusions (types A, B and C) cannot be calculated from microthermometric data alone. In addition, the volume proportions of the CO_2 and H_2O phases need to be estimated. The inclusions were therefore heated to 40°C , where all inclusions had become two-phase by homogenization of the CO_2 phase above its critical temperature (32°C). Both phases are assumed to have end-member composition; the H_2O phase is assumed to be incompressible with a density of 1 g cm^{-3} , and the density of the supercritical CO_2 phase at 40°C is determined by the isochore of pure CO_2 defined by Th_{CO_2} (Burrus, 1981). The area fractions of the CO_2 and H_2O phase were estimated from high-resolution images of the fluid inclusions taken at 40°C , using the image analysis software of the optical microscope. Area proportions were extrapolated to

volume fractions assuming a spherical shape for the bubbles and rounded isometric fluid inclusions, and a cylindrical shape for fluid inclusions with negative crystal shapes. From the volume fractions, the salinity and the CO_2 homogenization temperature, the bulk density and CO_2 mole fraction of the aqueous–carbonic fluid inclusions were calculated using the computer program BULK (Bakker, 2003).

The isochores for all fluid inclusions were calculated with the computer program ISOC (Bakker, 2003). Isochores of low- to intermediate-salinity aqueous inclusions were calculated from the empirical model for the H_2O –NaCl system (Driesner, 2007; Driesner & Heinrich, 2007), assuming that the influence of minor CO_2 is negligible. Isochores for more saline fluid inclusions were calculated with the equation of state of Zhang & Frantz (1987). For aqueous–carbonic fluid inclusions, the equation of state of Bakker (1999) was used, which is based on the model for the H_2O –NaCl– CO_2 system of Bowers & Helgeson (1983).

LA-ICP-MS measurements were performed with a Perkin Elmer Elan 6100 DRC quadrupole ICP mass spectrometer, of single fluid inclusions ablated with a beam-homogenized 193 nm excimer system (Geolas, ETH prototype; Günther *et al.*, 1998). In the fluid inclusions the following elements were measured: Na, Mg, Si, S, K, Ca, Mn, Fe, Cu, Zn, Cs, W and Cu. For S and Cu the dwell time was doubled to 20 ms to reduce the detection limits.

Data reduction and quantification were done with the computer program SILLS (Guillong *et al.*, 2008). Host mineral-corrected fluid inclusion signals were quantified relative to the external standard NIST-610 to obtain the concentration ratios of elements in the inclusion. From the concentration ratios and the microthermometrically determined NaCl eqv. wt %, absolute element concentrations are calculated, correcting for minor KCl and CaCl_2 measured by LA-ICP-MS (Heinrich *et al.*, 2003). The limit of detection was evaluated based on the standard deviation of the instrument background signals for each element in each inclusion. Where net inclusion intensities dropped below this significance limit, the maximum concentration of the element was calculated to a minimum significant intensity of three times the standard deviation (3σ) of the background (Longerich *et al.*, 1996; Heinrich *et al.*, 2003).

Fluid inclusion petrography

In the samples from Monte Mattoni, we observed a number of consistent fluid inclusion assemblages (FIA); that is, groups of coevally trapped fluid inclusions on single growth features (Goldstein & Reynolds, 1994). The samples mostly contain fluid inclusion assemblages in pseudo-secondary and secondary trails. We exclusively selected pseudo-secondary FIA (i.e. trails that do not cut through outermost growth zones) for microthermometry and LA-ICP-MS analysis. Based on textural relations, phase proportions and

microthermometric data, the FIA were combined into five distinct types (A–E). The earliest fluid trapped in fluid inclusions is most probably present in the ocelli and fluid pockets of the geologically older Mattoni gabbro. Ocelli samples indeed show fluid inclusions of one distinct type (type A). The subsequent, more evolved

fluid is trapped in fluid inclusions in miarolitic cavities of the geologically younger Cadino gabbro. **Figure 6** shows a single quartz crystal from a miarolitic cavity, where the occurrence and chronology of the different fluid inclusion assemblages on pseudosecondary trails were mapped in detail. The distribution of these

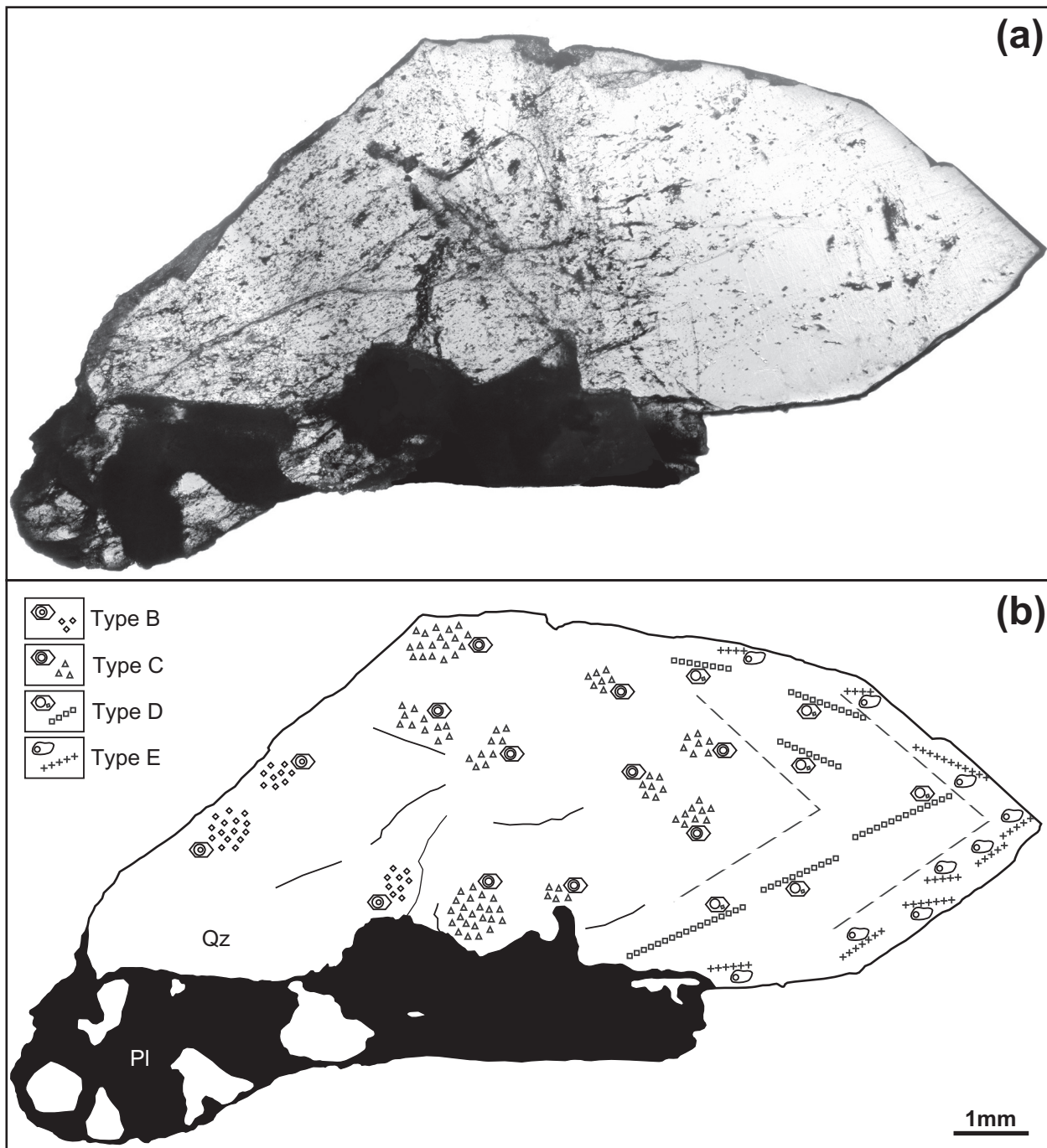


Fig. 6. Distribution of fluid inclusions in a partly free-standing euhedral quartz crystal (sample SHA-0709–42) from a miarolitic cavity, sampled near the top of Monte Mattoni in the Cadino gabbro. (a) Plane-polarized light photograph of the quartz crystal. The milky quartz at the base of the crystal that is intergrown with plagioclase (PI; now dark owing to saussuritic–propylitic alteration to albite and microscopic epidote), and the clear quartz at the freely grown top, should be noted. (b) Mapped fluid inclusion assemblages (types B–E) occurring within the crystal. The dashed lines indicate growth zones. The distinct occurrence of one fluid inclusion type within each growth zone should be noted.

inclusion types (B–E) in distinct growth zones of the quartz crystal suggests a clear relative time sequence regarding their entrapment.

Type A

The quartz crystals filling the ocelli and fluid pockets of the Mattoni gabbro preserve clear areas with aqueous–carbonic three-phase (LLV) fluid inclusions with a size up to 8 μm and rounded to irregular shape. They show very little aqueous liquid, a large volume fraction of liquid CO_2 and a small CO_2 gas bubble (Fig. 7). Because

only a few inclusions occur in a single area, it was not possible to establish consistent assemblages. However, these aqueous–carbonic fluid inclusions are texturally earlier than the abundant secondary aqueous inclusions of later types, aligned on microfractures crosscutting entire quartz crystals.

Types B and C

Quartz crystals in miarolitic cavities (Fig. 6) in the Cadino gabbro always show two main generations of quartz. The earlier quartz at the base of the crystal

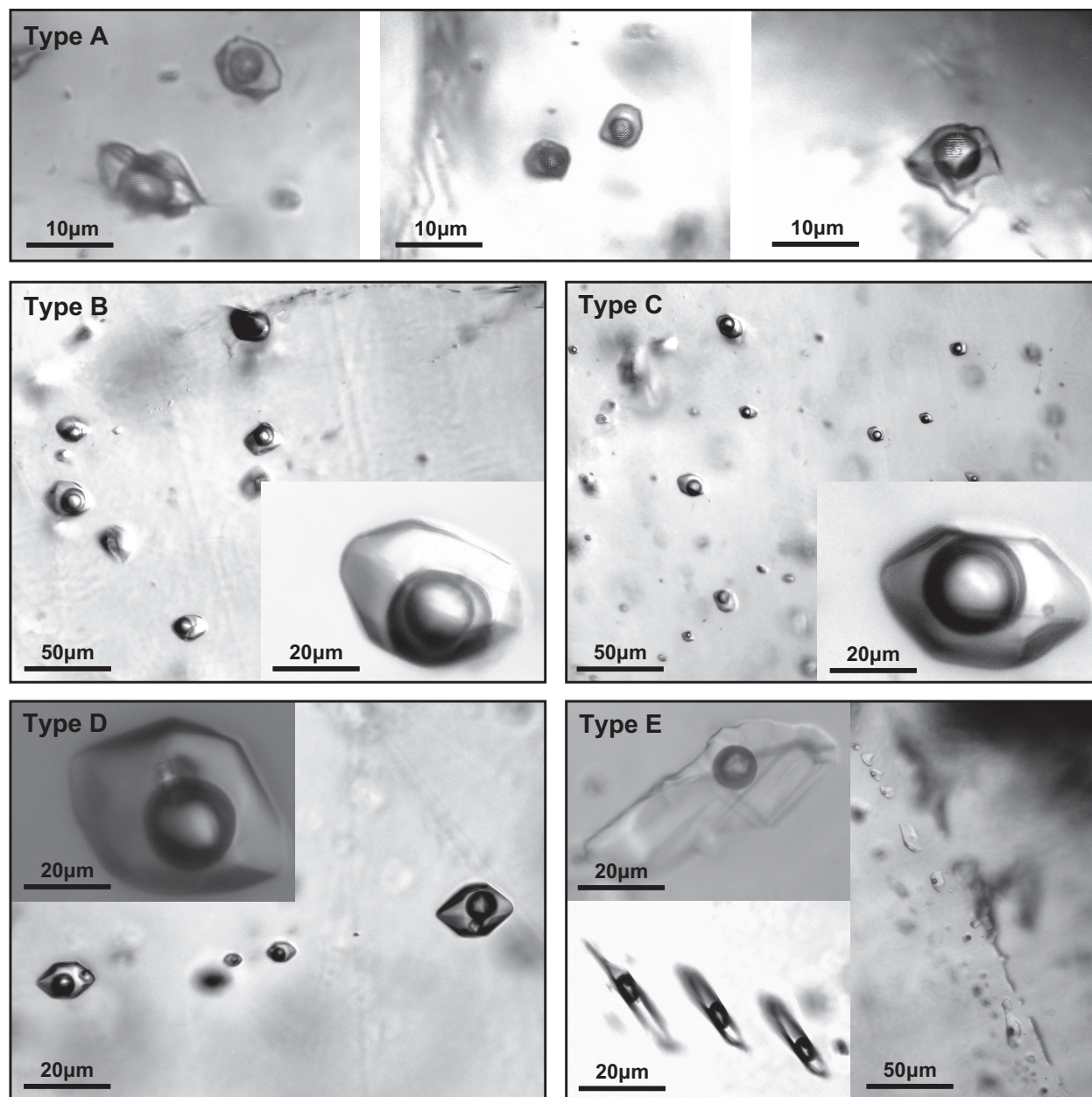


Fig. 7. Photomicrographs of the fluid inclusion types present within the Monte Mattoni mafic complex. Type A fluid inclusions are aqueous–carbonic, rounded to irregular in shape, around 5–10 μm in size and occur as clusters only in the ocelli and fluid pockets of the Mattoni gabbro. Types B and C are aqueous–carbonic, around 10–50 μm in size, have negative crystal shapes and appear in clusters. The difference in the CO_2 bubble size and the occurrence of tiny daughter crystals in type C fluid inclusions should be noted. Type D fluid inclusions are aqueous, 5–40 μm in size, have calcite daughter crystals and appear mainly on pseudo-secondary trails. Type E fluid inclusions are aqueous, irregular in shape, 10–60 μm in size and either occur on pseudo-secondary trails ending at, or within, the zone composed of quartz + chlorite, or they appear texturally primary.

appears milky, whereas the later quartz at the top is distinctly clear. Within the milky portion of the crystal, aqueous–carbonic fluid inclusions occur, which are never found in the clear part of the crystal, so these inclusions are clearly early pseudo-secondaries. They have a negative crystal shape and are up to 30 μm in size. The fluid inclusion assemblages close to the very base of the crystal (type B) have a slightly larger volume fraction of CO_2 than those occurring in the next central growth zone of the crystal, which are therefore differentiated as type C. The size of the CO_2 vapor bubble in type C inclusions is consistently larger than that in the type B inclusions (Figs 6 and 7). Type C inclusions contain tiny daughter crystals (Fig. 7), which were too small to be identified. Both type B and C inclusions occur in clusters in the early growth zones of the quartz crystal, but are never found in distinct trails. Because the fluid inclusions of type B occur always at the base of the crystal and show a higher fraction of CO_2 (similar to the fluid inclusions found in the ocelli and fluid pockets of the Mattoni gabbro), they are interpreted as being earlier than the fluid inclusions of type C.

Type D

In the clear portion of the quartz exclusively aqueous fluid inclusions are present. The growth zone that immediately follows the milky part of the crystal contains aqueous two-phase (LV type) inclusions that have negative crystal shape, a size of 5–30 μm and vapor bubble sizes of 10–15 vol. %. They contain small daughter crystals that have a rhombohedral shape and very high birefringence, suggesting calcite (Fig. 7). Assemblages of type D occur mainly on pseudo-secondary trails that do not crosscut the outermost growth zone. In this zone of the crystal, solid inclusions of epidote can also be found. Type D fluid inclusions were trapped subsequently to the aqueous–carbonic ones.

Type E

The outermost growth zone of the quartz crystal is commonly intergrown with chlorite. Stopping either before this growth zone or within it appear pseudo-secondary trails of aqueous LV fluid inclusions, 10–40 μm in size, with an irregular shape and vapor bubble sizes of about 5–10 vol. %. In the growth zone where type E fluid inclusions occur, no other types of fluid inclusions are found. Therefore, these inclusions trapped the latest fluids from the magmatic–hydrothermal system.

Microthermometric results

A summary of the microthermometric data and bulk fluid properties is given in Table 1, and the data are plotted in Fig. 8.

Type A

The fluid inclusions of type A are too small for reliable measurement of all phase transitions. In three inclusions the final melting of CO_2 could be consistently

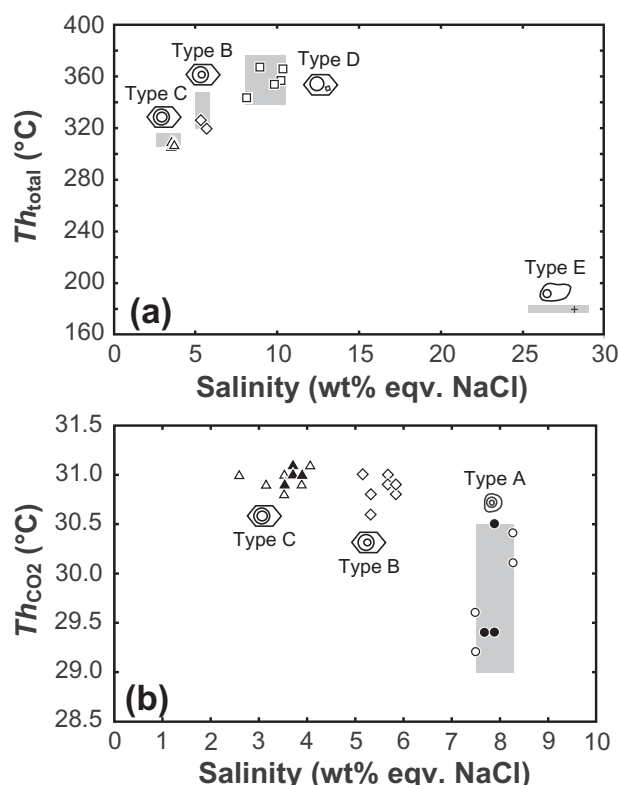


Fig. 8. Microthermometric data. (a) Salinity vs temperature of total homogenization of aqueous and aqueous–carbonic fluid inclusions (types B–E). The shaded areas give the full range in measured temperatures, including also data where only Th_{total} or the salinity was determined in a single fluid inclusion. (b) Salinity vs CO_2 homogenization temperature of the aqueous–carbonic fluid inclusions (types A–C). The shaded area gives the full range in measured temperatures, including also data points where Th_{CO_2} and the salinity could not be determined on the same inclusion. Filled and open symbols indicate data from different fluid inclusion assemblages. The carbonic phases in fluid inclusions of types A and B homogenize into the liquid phase, whereas in type C inclusions they homogenize to CO_2 vapor.

determined at $-56.9 \pm 0.2^\circ\text{C}$, whereas the final ice melting temperature could not be measured. The final melting of clathrate was measured in seven inclusions at $5.7 \pm 0.2^\circ\text{C}$. The CO_2 homogenization temperature into the liquid phase was determined in all inclusions at $29.4 \pm 0.7^\circ\text{C}$. It was not possible to measure the total homogenization of the inclusions.

Type B

The final melting of CO_2 is at $-56.6 \pm 0.1^\circ\text{C}$. Abundant clathrate finally melted at $7.1 \pm 0.1^\circ\text{C}$. The partial homogenization of CO_2 into the liquid phase occurs at $30.9 \pm 0.1^\circ\text{C}$ and the total homogenization at $334 \pm 10^\circ\text{C}$ into the liquid phase.

Type C

The final melting temperature of CO_2 in the fluid inclusions is at $-56.8 \pm 0.2^\circ\text{C}$. As in the fluid inclusions of type B, it was not possible to detect the final melting of ice. The final melting of clathrate takes place at

$8.2 \pm 0.2^\circ\text{C}$. The partial CO_2 homogenization into the vapor phase occurs at $31.0 \pm 0.1^\circ\text{C}$. The total homogenization occurs at $310 \pm 3^\circ\text{C}$ into the liquid phase.

Type D

These fluid inclusions are aqueous two-phase with very small calcite daughter crystals (Fig. 6). Microthermometric measurements show that they contain a small amount of CO_2 . The final CO_2 melting is clearly visible at $-57.1 \pm 0.1^\circ\text{C}$ and the final ice melting occurs at $-6.2 \pm 0.7^\circ\text{C}$ in the presence of a small amount of clathrate. In those inclusions where measurement of clathrate melting was possible it occurred at $9.1 \pm 0.3^\circ\text{C}$. These observations indicate a small fraction of CO_2 and justify estimation of salinity for fluid inclusions of type D based on the final ice melting temperature. The total homogenization into the liquid phase was measured at $353 \pm 11^\circ\text{C}$.

Type E

The initial ice melting temperatures in these fluid inclusions were around -60°C and the final ice melting took place at $-27.5 \pm 1.4^\circ\text{C}$; that is, well below the H_2O – NaCl eutectic at around -21°C . This indicates that these inclusions contain other major solutes, most probably CaCl_2 (as confirmed by LA-ICP-MS; see below). The total homogenization temperature could be determined in only one inclusion at 179°C (into the liquid phase), in line with the consistently tiny bubble size of all others that leaked during heating.

Evolution of bulk fluid properties

The bulk properties of the aqueous–carbonic fluid inclusions show three distinct features, as follows: (1) the different fluid inclusion assemblages show consistent data; (2) the salinity of the aqueous–carbonic fluid inclusion types decreases with time (Fig. 8a); (3) the CO_2 mole fraction decreases with some overlap from type A through type B to type C and the CO_2 -free type D and E inclusions. The earliest type A fluid inclusions in the ocelli have a salinity of 7.9 ± 0.3 wt % eqv. NaCl . Fluid inclusions of type B at the base of the quartz crystal in the miarolitic cavities show a salinity of 5.5 ± 0.3 wt % eqv. NaCl , and the subsequent fluid inclusions of type C have a salinity of 3.6 ± 0.4 wt % eqv. NaCl . After this correlated decrease in CO_2 and salt content from A to C, salinities increase again (Fig. 8b). Aqueous type D fluid inclusions have a salinity of 9.5 ± 1 wt % eqv. NaCl , which is higher than the salinity of the earliest type A inclusions. Type E inclusions have a salinity of 27.1 ± 0.9 wt % eqv. NaCl , indicating a major increase in the salinity of the aqueous fluid inclusion types with time. The total homogenization temperatures do not correlate with the salinity.

Final CO_2 melting temperatures in the range between -57.1 and -56.6°C indicate that all aqueous–carbonic inclusion types contain essentially pure CO_2 , without additional volatiles such as CH_4 or N_2 (Hollister & Burrus,

1976; Touret, 1982; Thiery *et al.*, 1994). The X_{CO_2} decreases from the early aqueous–carbonic fluid inclusions to the late aqueous fluid inclusions. Type A fluid inclusions have a CO_2 fraction of 0.14, whereas X_{CO_2} values in type B and C inclusions are 0.11 and 0.06, respectively. Type D inclusions contain only trace amounts of CO_2 , whereas type E inclusions contain no detectable CO_2 . The bulk density decreases continuously from type A (0.91 g cm^{-3}) to type D (0.73 g cm^{-3}), and increases again in type E (1.1 g cm^{-3} ; Fig. 9).

LA-ICP-MS data

Nine well-constrained fluid inclusion assemblages of inclusion types B–E were measured using LA-ICP-MS. Type A inclusions were too small for successful analysis. Overall, good agreement of the measured element concentrations within one fluid inclusion assemblage and between different assemblages of one fluid type can be observed (Table 2, Fig. 10). For comparison the data from each fluid inclusion type were averaged and plotted on a normalized trace element diagram (Fig. 11). The concentration of Mg is consistently low (20–30 ppm) and identical within the scatter among fluid inclusion types B–D, but increases in type E inclusions (100 ppm). The concentration of K increases systematically from 0.15 wt % in inclusion types B and C to 0.62 wt % in type D inclusions, and further to 1.07 wt % in type E inclusions. Ca shows a similar but more substantial increase in the later fluid inclusion types.

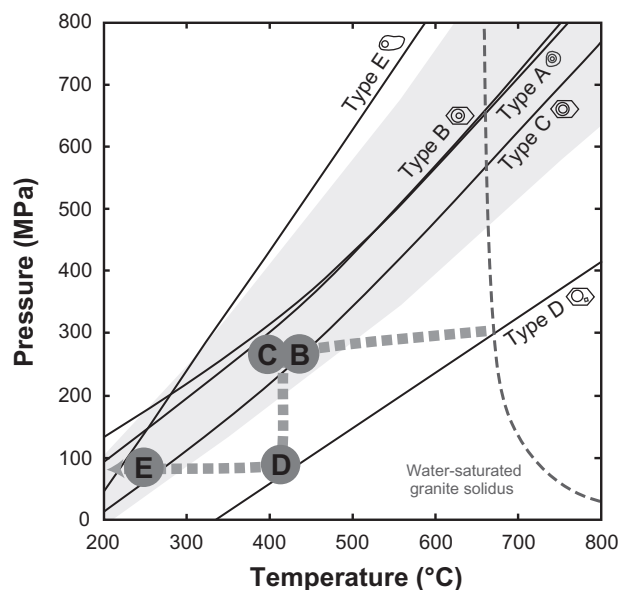


Fig. 9. Pressure–temperature diagram showing isochores for the five fluid inclusion types at the Monte Mattoni mafic complex, the water-saturated solidus for natural granites, the estimated P – T conditions for entrapment of fluid inclusion types (circles labeled with letters B–E) and the P – T path (bold dashed line) of the fluid inferred from the relative chronology of the fluid inclusions. The shaded wedge illustrates the full permissible range in isochore position for aqueous–carbonic type A, B and C fluid inclusions, taking into account the uncertainty of the density calculation from estimated volume fractions of CO_2 .

Table 2: Element concentrations (ppm) obtained from LA-ICP-MS analysis of fluid inclusion assemblages (FIA) from fluid inclusion types B–E

FIA	Na	Mg	S	K	Ca	Mn	Fe	Cu	Zn	Cs	W	Pb
<i>Sample SHA-0709–42, FI type B</i>												
B1	19000	28	300	2000	3200	330	330	120	80	2.9	<0.9	120
	15200	210	3000	12000	<3100	18	2100	1300	30	2.8	<1.3	40
	21100	<3	1000	1200	<1600	160	36	520	20	4.6	0.7	60
	20400	38	680	1200	<1100	260	93	190	20	5.7	<0.4	15
	20900	16	280	1600	<1200	360	220	260	90	4.2	<0.5	120
<i>Sample SHA-0709–42, FI type C</i>												
C1	13600	<12	2800	2600	<10700	170	1900	3200	110	3.1	<3.4	40
	8400	33	800	1200	10500	6	160	80	<6	3.6	2.6	12
	12700	<2	1200	1200	2300	11	28	200	<1	3.1	0.9	4.1
	13900	<3	1500	980	<3100	28	<50	140	9	2.9	<1.2	7.1
	11000	<3	2100	1400	5600	12	100	140	13	2.1	<0.7	12
C2	13400	13	2900	1000	<1400	39	160	360	5	4.8	0.8	1.8
	13400	<2	1100	970	<1100	40	96	250	2	1.5	<0.4	2.0
	12500	16	1000	1200	<2000	20	180	230	<3	2.7	<0.9	4.8
	12300	9	2300	670	2200	19	100	740	2	3.6	<0.4	2.0
<i>Sample SHA-0709–42, FI type D</i>												
D1	30900	13	420	5200	9400	1070	3000	50	370	4.3	<1.6	170
D2	36300	28	<20	6400	3300	330	760	80	70	20.4	<0.3	150
	35100	42	78	7000	4800	850	2100	140	130	6.3	0.2	200
	36600	8	88	7000	2100	560	1700	30	320	7.6	0.4	190
	35600	12	180	6200	4500	340	350	80	280	7.0	<0.3	200
D3	29000	23	82	5200	6300	800	1700	140	260	6.8	<0.3	150
	29500	18	200	6500	4500	480	750	80	240	7.9	<0.4	170
	30100	15	88	6300	2300	300	680	80	120	11.4	<0.3	110
<i>Sample SHA-0709–44, FI type E</i>												
E1	42400	34	260	8800	108000	670	45	1.9	860	45	<0.6	360
	47200	61	180	10200	98000	1000	280	1.3	1100	48	<0.9	580
	46600	164	280	10200	99000	2200	120	<0.9	1100	54	<0.8	490
	48800	341	<49	10200	94400	2400	140	1.7	1300	56	1.1	600
E2	46700	1714	<320	8600	99400	2100	170	<3.7	750	43	<2.9	410
	45500	40	220	9900	103400	38	60	0.6	570	39	<0.2	250
	43500	62	220	9700	106800	160	34	0.9	860	46	<0.3	350
E3	48300	46	410	16100	99100	380	150	<2.4	430	53	<1.8	280
	62000	47	<320	13000	75000	3000	400	<3.1	1500	49	<2.8	870

The Ca concentration is in the range 0.3–0.5 wt % in inclusion types B–D, and increases to 9.8 wt % in the late type E inclusions. Remarkably, Ca is comparable with or even higher than Na in the late type E inclusions, consistent with their low final ice melting temperatures (Oakes *et al.*, 1990). The Cs concentration also increases from early aqueous–carbonic fluid inclusions to the later aqueous types, but with overall rather low values of 3–50 ppm.

The concentration of S in the aqueous–carbonic inclusion types B and C lies in the range 1000–2000 ppm, significantly higher than in the later aqueous fluid inclusion types D and E (around 200 ppm). This decrease in S over time is accompanied by a similar decrease in the concentration of Cu. Inclusion types B and C have Cu concentrations of 500 ppm, whereas those of type D have only 90 ppm. Cu concentrations in type E inclusions are below the limit of detection (a few ppm). By contrast, Zn and Pb have low concentrations in the early aqueous–carbonic fluid inclusions (10–70 ppm). Their concentrations increase significantly in the late aqueous fluid inclusions, with 200 ppm Pb and 900 ppm Zn in type D, reaching 500 ppm Pb and 900 ppm Zn in type E inclusions. The metals Fe and Mn show overall low concentrations in the range of 50–500 ppm, except for somewhat elevated Fe concentrations in type D

(1400 ppm) and Mn concentrations in type E (1300 ppm).

The solute concentrations of inclusion types B–E evolve along a trend that is consistent with the observed changes in bulk fluid properties. The concentrations of Na, Ca, K and Mg increase from the early aqueous–carbonic fluid inclusions (types B and C) to the later aqueous inclusions (types D and E). In particular, the Ca/Na ratio increases substantially in the aqueous fluid inclusion types and the latest type E inclusions are calcic–sodic brines. This main trend is accompanied by an increase in Pb and Zn, whereas Cu and S concentrations decrease from the aqueous–carbonic to the aqueous fluid inclusions. Subsequently, we will show that these systematic variations can be explained by initial fluid–melt partitioning of volatiles in the crystallizing magma, followed by sub-solidus reaction of isolated fluid pockets with the local rocks.

THERMODYNAMIC MODELING OF FLUID–MINERAL EQUILIBRIA

Here we explore to what extent the recorded fluid compositional variations can be explained by re-equilibration of magmatic–hydrothermal fluids with the local rock and its retrograde alteration observed around

the miarolitic cavities, or whether the large variations in salinity, CO₂ content and cation ratios require interaction of magmatic–hydrothermal fluids with an externally infiltrating brine; for example, from the

surrounding contact-metamorphosed metasediments (Floess & Baumgartner, 2015). To link the changes in fluid chemistry with changes in system parameters such as pressure, temperature and oxidation state, we have thermodynamically modeled fluid speciation and fluid–mineral equilibria considering a closed system at variable fluid/rock ratios, as a first-order test. All calculations were performed with the GEM-Selektor Gibbs free energy minimization package (Wagner *et al.*, 2012; Kulik *et al.*, 2013), which uses an interior point global optimization method to evaluate phase stability and speciation (Karpov *et al.*, 1997; Kulik *et al.*, 2013).

Source of thermodynamic data

The thermodynamic dataset covers all the main aqueous species, rock-forming minerals and their solid-solutions in the Si–Al–Fe–Mg–Ca–Na–K–C–H–O–Cl system. It is based on the model used by Dolejs & Wagner (2008), with additions for aqueous carbon species, carbonate minerals and their solid-solutions. Thermodynamic properties of the water solvent were calculated with the IAP–84 equation of state (Kestin *et al.*, 1984) and those of aqueous species with the modified Helgeson–Kirkham–Flowers (HKF) model (Helgeson & Kirkham, 1976; Helgeson *et al.*, 1981; Tanger & Helgeson, 1988). Data for charged and neutral aqueous species (Shock & Helgeson, 1988; Shock *et al.*, 1989, 1997; Johnson *et al.*, 1992; Sverjensky *et al.*, 1997) were augmented by critically evaluated data for aluminum species, HCl⁰ and MgCl₂⁰ (Tagirov *et al.*, 1997; Tagirov & Schott, 2001; Dolejs & Wagner, 2008). The end-member data for rock-forming minerals were taken from the internally consistent database of Holland & Powell (1998). This dataset, in conjunction with the aqueous species data reviewed above, reproduces measured mineral solubilities at elevated *T* and *P* within experimental uncertainty (Holland & Powell, 1998; Hauenberger *et al.*, 2002; Pak *et al.*, 2003).

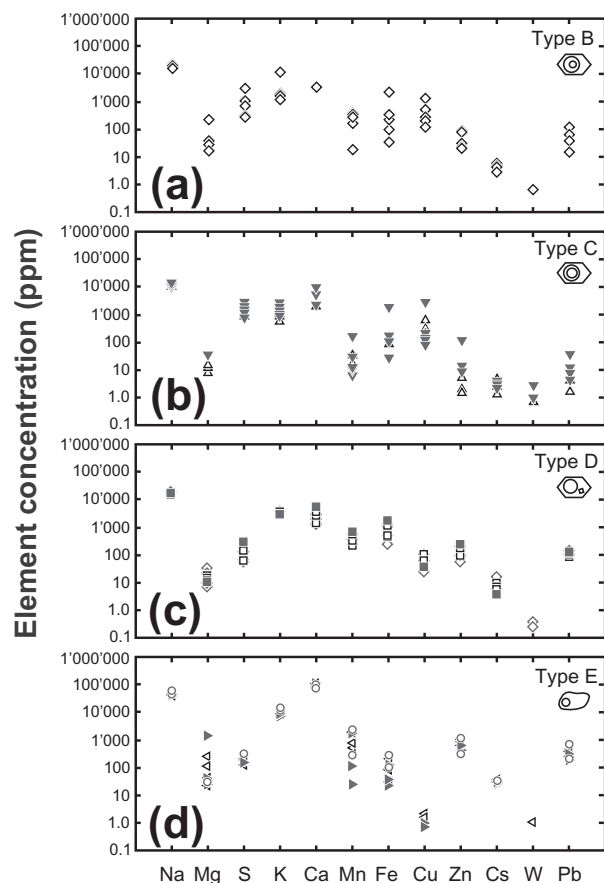


Fig. 10. Element concentrations (in ppm) of the four fluid inclusion types occurring in the miarolitic cavities of the Cadino gabbro. Symbols and fill patterns indicate the different fluid inclusion assemblages.

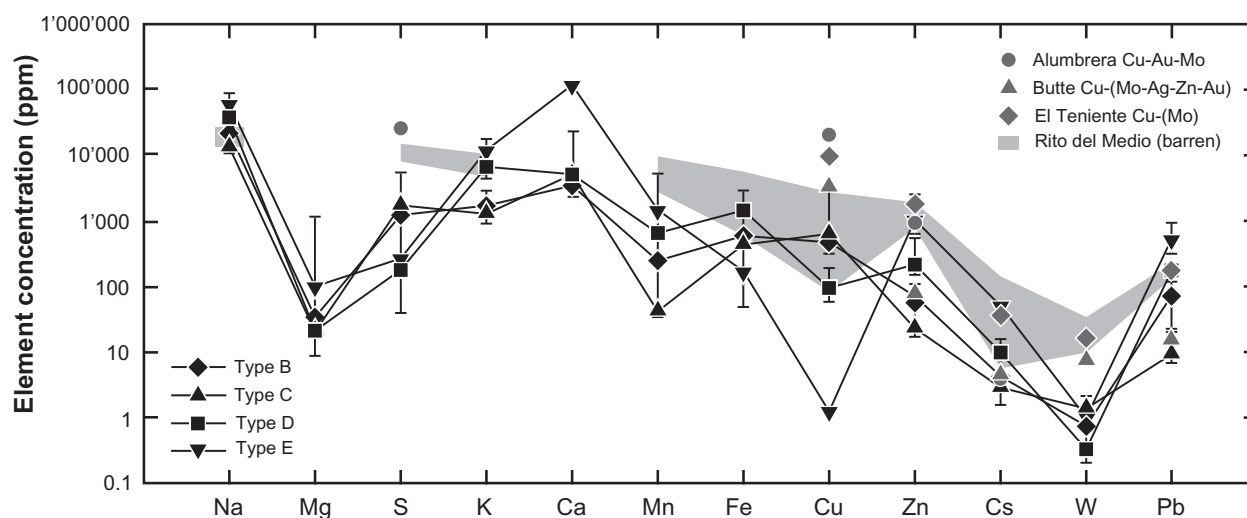


Fig. 11. Average element concentrations for each analyzed fluid inclusion type from the Monte Mattoni mafic complex (inclusion types B–E; error bars 1SD). For comparison, data from the barren Rito del Medio granite and three ore deposits (Bajo de la Alumbra Cu–Au–Mo, Butte Cu–(Mo–Ag–Zn–Au), El Teniente Cu–(Mo)) are also shown. Data sources: Ulrich *et al.* (2002), Rusk *et al.* (2004), Williams-Jones & Heinrich (2005), Klemm *et al.* (2007), Audétat *et al.* (2008) and supplementary sulfur data from Seo *et al.* (2009).

Activity–composition relationships for mineral solid-solutions were described by ideal, non-ideal symmetric and asymmetric models (Powell & Holland, 1993, 1999; Holland & Powell, 1996, 1998, 2003; Holland *et al.*, 1998; Coggon & Holland, 2002; Wei *et al.*, 2003; Dale *et al.*, 2005; Warren & Waters, 2006). Aqueous activity coefficients were calculated with the extended Debye–Hueckel equation and the activity coefficient of H₂O from the osmotic coefficient (Helgeson *et al.*, 1981; Walther, 1997, 2001). The extended Debye–Hueckel model is not strictly valid for saline brines (Pitzer, 1995), but recent conductance measurements in moderately concentrated NaCl and KCl solutions (to 4.5 mol kg^{−1}) at temperatures and pressures up to 600°C and 300 MPa have shown that it provides a good data representation within experimental uncertainty (Sharygin *et al.*, 2002).

Model design and input data

Fluid–mineral equilibria calculations were run along two isobaric paths (250 and 100 MPa) over the cooling range from 700 to 200°C, covering the transition from late-magmatic to hydrothermal conditions, consistent with observational constraints. The model pressures cover a comparatively large range, because the pressure of emplacement of the Mattoni and Cadino gabbros is not well constrained. Blundy & Sparks (1992) assumed a pressure of 250 MPa based on hornblende thermobarometry, which appears reasonable considering the likely thickness of overburden at the time of emplacement of the Mattoni and Cadino gabbros. Calculations were performed for a range of initial fluid/rock ratios (on a mass basis) from 0.035 to 0.10. These cover conditions from minimum estimates for H₂O solubility in gabbroic and granitic magmas saturated with amphibole (about 3–4 wt % H₂O) (Holtz *et al.*, 1995, 2001; Clemens & Watkins, 2001), to the presence of excess fluid owing to the segregation of fluid pockets into miarolitic cavities in contact with a restricted halo of igneous rock. The fluid/rock ratio and chlorinity of the fluid were allowed to change along the simulation path owing to transfer of H₂O between the fluid and the rock, notably the formation of hydrous silicate minerals, with chloride considered as a conservative component residing in the fluid only.

The bulk-rock composition used in the modeling was taken from a representative whole-rock analysis of the Cadino gabbro (sample CAD-3; Ulmer, 1986) that included determination of the Fe³⁺/Fe²⁺ ratio. The bulk-rock composition was converted to SiO₂–Al₂O₃–Fe₂O₃–FeO–MgO–CaO–Na₂O–K₂O composition space by subtracting stoichiometric amounts of FeO and CaO bound in ilmenite and apatite, respectively, to account for analyzed TiO₂ and P₂O₅ concentrations. Subsequently, the whole-rock composition was normalized to 100 wt % on a volatile-free basis (Table 3). The initial fluid composition was derived from the average composition of type B fluid inclusions (earliest growth zone in miarolitic

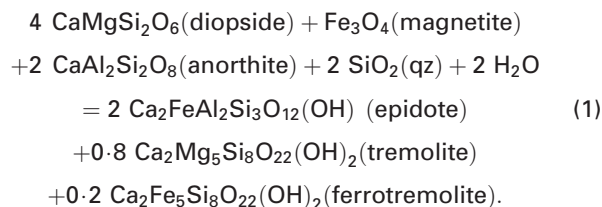
Table 3: Original (Ulmer, 1986) and recalculated whole-rock compositions (wt %) used for fluid–mineral equilibria modeling

Sample:	CAD-3 Cadino gabbro (original data)	CAD-3 Cadino gabbro (recalculated)
SiO ₂	51.55	54.05
TiO ₂	0.96	0
Al ₂ O ₃	15.82	16.59
Fe ₂ O ₃	1.94	2.03
FeO	5.55	4.92
MnO	0.17	0
MgO	7.48	7.84
CaO	10.99	11.46
Na ₂ O	2.29	2.41
K ₂ O	0.66	0.69
P ₂ O ₅	0.10	0
H ₂ O	1.96	0
CO ₂	0.17	0
Total	99.64	100.00

cavities in the Cadino gabbro), obtained from the combination of microthermometric and LA-ICP-MS data. The recalculation into solute molalities is straightforward in the case of H₂O–NaCl inclusions, but requires simultaneous solution of a linear set of equations in the case of H₂O–CO₂–NaCl inclusions (see Appendix A). The recalculation scheme was based on two simplifying assumptions: (1) that the common salt correction (Heinrich *et al.*, 1992) is applicable to aqueous calcic brines and aqueous–carbonic fluid inclusions; (2) that the concentration of ligands other than Cl in the fluid inclusions is negligible.

Modeling results

Figures 12 and 13 summarize the total element solubilities and major fluid parameters (pH, oxidation state, Ca/Na ratio, K/Na ratio, CO₂/Cl ratio) over the temperature range 300–700°C and at 250 MPa. At 700°C, the initial mineral assemblage is calcic plagioclase, amphibole, biotite, clinopyroxene, magnetite and quartz (Table 4), consistent with the observed magmatic mineralogy. With decreasing temperature, several important mineral transformations result in sharp changes in the solubility curves (Fig. 12). At 540–550°C, clinopyroxene is converted to epidote by the reaction



This reaction consumes quartz and H₂O, resulting in a slight increase in salinity. After the reaction has been intersected, the solubilities of both Fe and Mg change slope from positive to negative temperature dependence (Fig. 12). Fluid pH (Fig. 13a), oxidation state (Fig. 13b) and the K/Na ratio (Fig. 13d) decrease

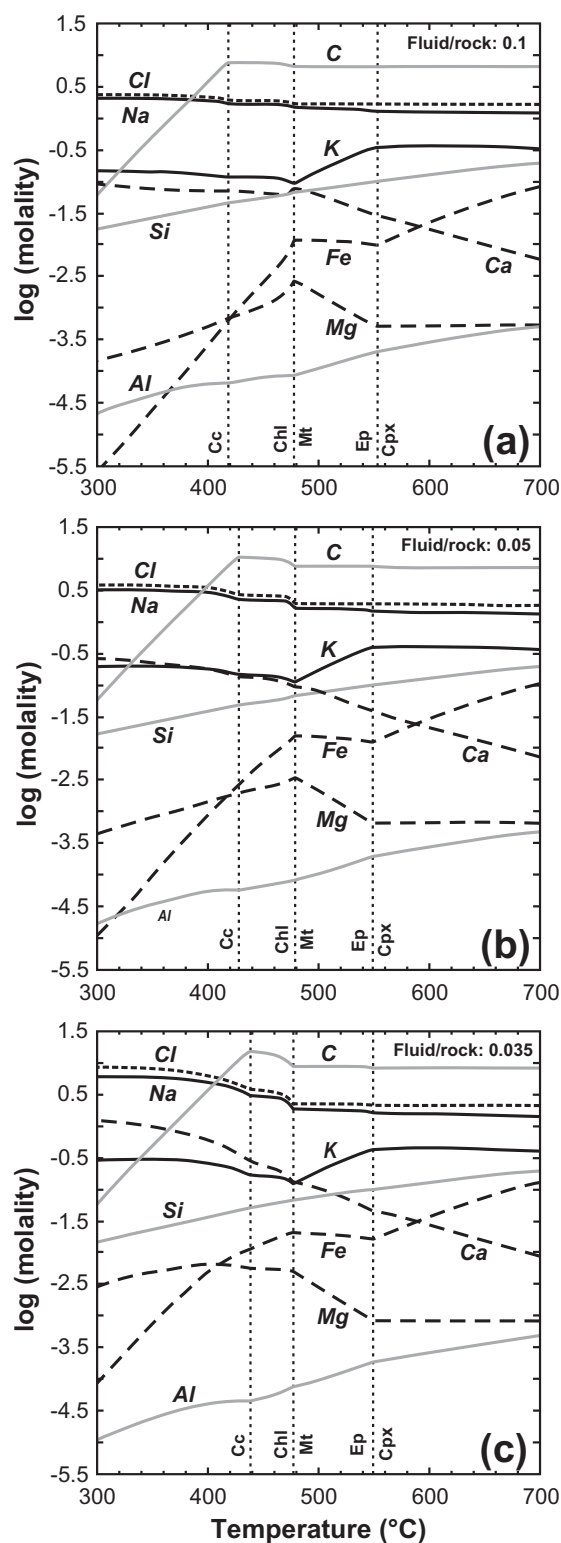


Fig. 12. Results of fluid–mineral equilibria modeling predicting the temperature dependence (at 250 MPa) of fluid composition, expressed as total dissolved element molalities (sum of all species molalities of a given element; lines). Calculations were performed at fluid/rock ratios of (a) 0.1, (b) 0.05 and (c) 0.035. Mineral abbreviations: Cc, calcite; Chl, chlorite; Mt, magnetite; Ep, epidote; Cpx, clinopyroxene.

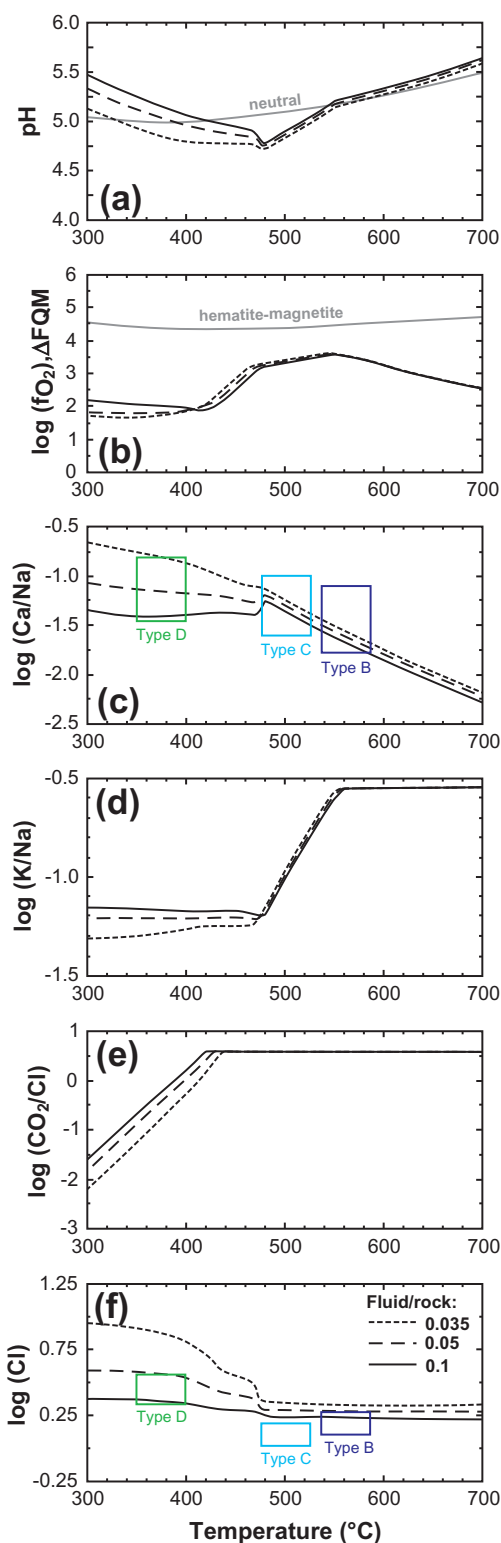
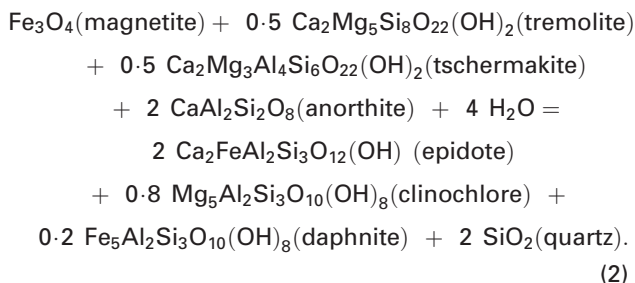


Fig. 13. Modeled evolution of (a) pH, (b) oxygen fugacity [relative to fayalite–quartz–magnetite (FQM) buffer], (c) log (Ca/Na), (d) log (K/Na), (e) log (CO₂/Cl) and (f) log (Cl) as a function of temperature at 250 MPa.

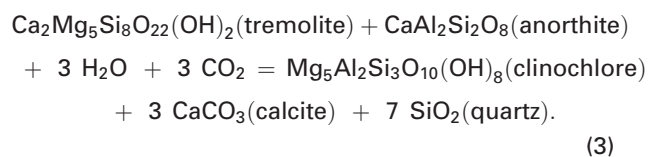
Table 4: Summary of the modeled mineral assemblages as a function of temperature and pressure

<i>T</i> (°C)	<i>P</i> (MPa)	Mineral assemblage
<i>Simulation 1</i>		
700	250	plag + amph + bt + cpx + mt + qz
540–550	250	plag + amph + bt + ep + mt + qz
470–490	250	plag + amph + bt + ep + chl + qz
410–430	250	plag + amph + bt + ep + chl + qz + cc
<i>Simulation 2</i>		
500	100	plag + amph + bt + ep + mt + qz
420–440	100	plag + amph + bt + ep + chl + qz
400–410	100	plag + amph + bt + ep + chl + qz + cc
270–280	100	plag + amph + bt + ep + chl + qz + cc + pre
230–250	100	plag + amph + ep + chl + qz + cc + pre

substantially. The next important mineral transformation occurs at 470–480°C, where magnetite reacts to form chlorite:



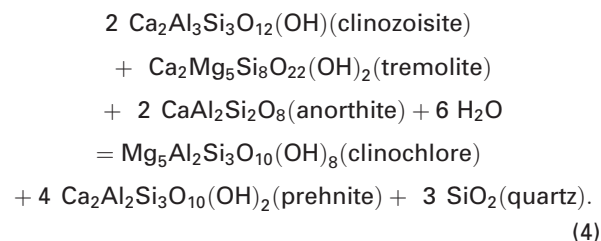
The reaction produces additional epidote and quartz and consumes amphibole (tremolite and tschermakite components), anorthite and H₂O. Fluid pH (Fig. 13a) and K/Na ratio (Fig. 13d) reach a minimum at this point, and the solubility curves of Mg, Fe and Ca change slope. The CO₂ concentration in the fluid remains essentially constant, until at temperatures of 410–430°C calcite is precipitated by the reaction



This reaction consumes amphibole, plagioclase (anorthite component), H₂O and CO₂, and results in formation of large amounts of quartz and calcite. The precipitation of calcite causes a sharp inflection point in the CO₂ solubility curve (Fig. 12), with the CO₂ concentration dropping by several orders of magnitude with further temperature decrease (Fig. 13e). As reactions (2) and (3) consume anorthite, the plagioclase becomes increasingly sodic with decreasing temperature. Major changes in fluid chemistry in response to rock-buffered fluid cooling at 250 MPa are a sharp decrease in K/Na ratio at higher temperatures, progressive increase in Ca/Na ratio with decreasing temperature and a substantial drop in CO₂ solubility and CO₂/Cl ratio at temperatures below 350–400°C (Fig. 13). At temperatures above 480°C, the modeling results are essentially independent

of the fluid/rock ratio, whereas at lower temperatures the fluid pH (Fig. 13a), the Ca/Na ratio (Fig. 13c) and the total salinity (Fig. 13f) are strongly affected. Fluid evolution towards calcic–sodic brines via fluid–rock reaction requires a low fluid/rock ratio of 0.035, lowered further by H₂O consumption.

The simulation at 100 MPa shows similar trends at higher temperatures, but some additional features at temperatures below 400°C (Fig. 14). Most element solubility curves show smooth trends in the temperature range 300–400°C, but important changes occur around 270–280°C owing to a mineral reaction that consumes epidote (clinozoisite component), amphibole and plagioclase to form chlorite and additional prehnite:



This reaction results in a substantial change in the slope of the Fe and Mg solubility curves (Fig. 14). In addition, the Ca/Na ratio (Fig. 15c) and the oxidation state (Fig. 15b) of the fluid increase sharply. The increase in oxidation state at lower temperatures is probably related to a change in the buffering assemblage involving ferrous and ferric end-members in epidote and chlorite solid-solutions. The most remarkable changes in fluid chemistry at low temperatures are the strong increases in bulk salinity and Ca/Na ratio. This results in formation of very saline brines (of the order of 8–12 mol kg^{−1} Cl) that have high Ca/Na ratios in the range of 0.5–1.0. These two compositional effects are most pronounced at the lowest initial fluid/rock ratio of 0.035, and less prominent at higher fluid/rock ratios of 0.05 and 0.1 (Fig. 15c and f).

DISCUSSION AND CONCLUSIONS

Petrographic observations and fluid inclusion data demonstrate that two distinct fluid saturation events occurred during the evolution of the Monte Mattoni complex. The systematic decrease in CO₂ concentration, the decrease and subsequent increase in salinity, and the final rise of Ca/Na ratio in the latest aqueous brines can be explained by successive distillation of a magmatic–hydrothermal fluid from a crystallizing magma (fluid generations A–C) and subsequent subsolidus re-equilibration of locally trapped fluid pockets with the surrounding host-rock (fluid generations D–E).

P–T evolution from lithostatic to hydrostatic conditions

Representative isochores for inclusion types A, B and C (Fig. 9) are located in a narrow sector, even if maximum uncertainties in the estimated densities (CO₂ volume

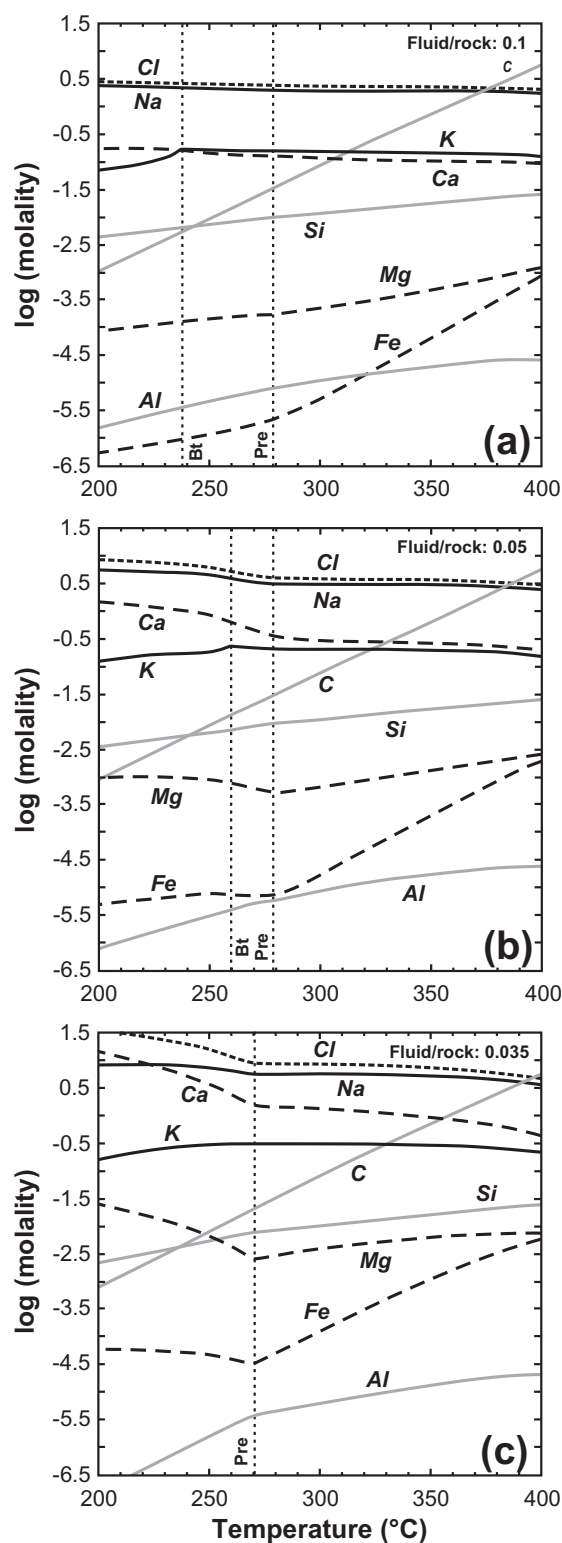


Fig. 14. Temperature dependence of the fluid composition (at 100 MPa) at fluid/rock ratios of (a) 0.1, (b) 0.05 and (c) 0.035. Mineral abbreviations: Pre, prehnite; Bt, biotite.

fraction estimates, equations of state used) are considered. They suggest that the earlier fluid generations were trapped at similar P - T conditions. Considering that even the earliest fluid types exsolved from melts in

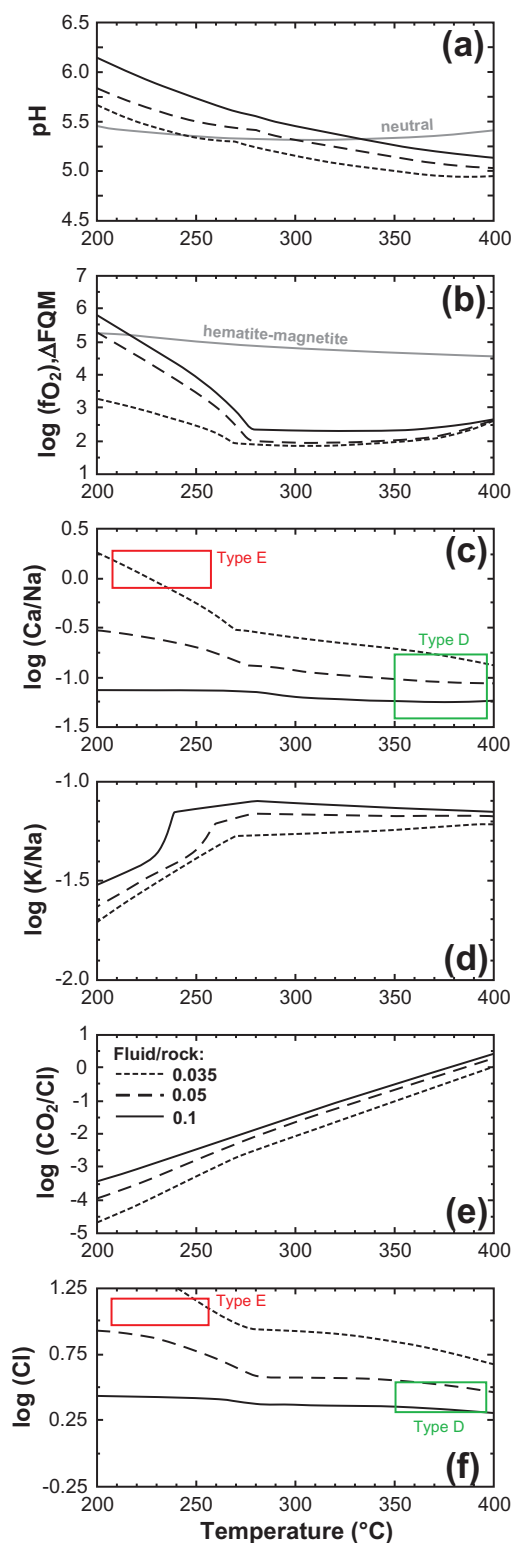


Fig. 15. Modeled evolution of (a) pH, (b) oxygen fugacity (relative to FQM buffer), (c) $\log(\text{Ca/Na})$, (d) $\log(\text{K/Na})$, (e) $\log(\text{CO}_2/\text{Cl})$ and (f) $\log(\text{Cl})$ as a function of temperature at 100 MPa. Rectangles indicate analyzed compositions of fluid inclusions.

pockets associated with pegmatitic and locally graphic textures, these fluid inclusions were probably trapped when the melt pockets crystallized under conditions of significant (100–300°) undercooling below the liquidus

temperature (London, 2005, 2009). Accepting independent lithostatic pressure estimates of *c.* 250 MPa for the emplacement of the Adamello batholith (Blundy & Sparks, 1992), reasonable estimates for the trapping temperature of fluid inclusion types A–C of 500–550°C result from the calculated inclusion isochores (Fig. 9). This *P–T* estimate is in turn consistent with the modeling of fluid–mineral equilibria, which predict the first appearance of epidote (at the expense of clinopyroxene) at around 540–550°C, observed as inclusions in quartz crystals just prior to the entrapment of type D inclusions.

The transition from type C to type D fluid inclusions records a major change in the *P–T* evolution of the fluid system. Isochores constructed for type D inclusions have a much flatter slope than those of the aqueous–carbonic fluid inclusion types trapped earlier (Fig. 9). This requires a significant drop in fluid pressure reflecting, most probably, a change from lithostatic to near-hydrostatic pressure conditions. The subsequent evolution towards the trapping conditions of the type E inclusions records further cooling at near-isobaric conditions. Model predictions match the observation that growth zones in miarolitic quartz hosting type E fluid inclusions as cross-cutting trails contain exclusively chlorite as mineral inclusions. This demonstrates that chlorite formed subsequent to the entrapment of type D inclusions and prior to type E inclusions. The fluid–mineral equilibria modeling predicts that chlorite appears at 470–480°C at 250 MPa, and at 420–440°C at 100 MPa. In conjunction with the calculated isochores these mineral phase relations constrain the entrapment conditions of type E inclusions to 200–300°C and 100 MPa or less.

Chemical evolution of fluids

The initial decrease in salinity recorded by the transition from type A to type B and C inclusions (from 7.9 to 5.5 and 3.6 wt % NaCl) can be readily explained by changes in the chlorine partitioning between silicate melt and the exsolving fluid. The relative partitioning of chloride and water is pressure dependent (Kilinc & Burnham, 1972; Cline & Bodnar, 1991), and at pressures of 200 MPa and above, high partition coefficients for Cl in favor of the fluid phase result in the initial exsolution of more saline brines. With progressive crystallization and fractionation the remaining melt becomes increasingly depleted in Cl and successively exsolved batches of magmatic–hydrothermal fluid will therefore have lower Cl concentrations (Cline & Bodnar, 1991). This explanation also matches the concurrent decrease in CO₂ concentrations from X_{CO_2} of 0.14 in type A fluids to 0.11 and 0.06 in type B and C fluids. The first batch of fluid that exsolves from a CO₂–H₂O-bearing melt will contain the highest concentration of the more volatile CO₂ compared with the fluid exsolving at a later stage (Holloway & Blank, 1994; Papale *et al.*, 2006; Hsu, 2016). The quantity of early exsolving CO₂-rich fluid is limited by the small solubility of CO₂ in silicate melt (Webster, 2004),

consistent with the textural evidence indicating that the ocelli containing this fluid formed as a result of magma decompression during ascent and emplacement of the porphyritic Matttoni gabbro.

Further decrease in CO₂ concentration observed in the later aqueous fluid inclusion types (D and E) can be related to subsolidus precipitation of calcite, observed as a late-stage filling in ocelli and vugs in miarolitic pockets. This interpretation is supported by the results of fluid–mineral equilibria modeling, which predict calcite formation at the expense of Ca-rich silicates at 400–430°C, resulting in a drop in CO₂ concentration in the aqueous fluid phase by about three orders of magnitude during cooling from 400°C to 200°C. The texturally latest type E fluid inclusions do not contain any detectable CO₂, consistent with the thermodynamic calculations.

The subsolidus aqueous fluid inclusions show a reversal towards increasing salinity, reaching a maximum of 27 wt % eqv. NaCl in type E inclusions. This increase in salinity is coupled with a substantial increase in the Ca/Na ratio, and type E inclusions are essentially calcic–sodic brines. Both trends observed in the aqueous fluid inclusions can be quantitatively explained by equilibration of locally trapped fluid with a relatively large quantity of host-rock at around 250°C, with cation ratios being identical within analytical error to those measured by microthermometry and LA-ICP-MS. The strong increase in salinity and Ca/Na ratios in late-stage fluids is the consequence of progressive formation of hydrous silicate phases (epidote, chlorite) at the expense of anhydrous minerals. Plagioclase becomes unstable in the presence of a high-salinity fluid at lower temperatures, which results in progressive albitization near miarolitic cavities and release of Ca to the fluid (see Fig. 4d). Low-temperature alteration could also partly explain the presence of sodic rims (An₁₅) on calcic plagioclase (An₉₆) of the Cadino gabbro, although magmatic fractionation would equally result in crystallization of progressively more Ab-rich plagioclase (Blundy & Shimizu, 1991). The modeling results are a sensitive indicator of the integrated fluid/rock ratio. Formation of the observed calcic brines requires fluid/rock ratios of 0.02–0.05, which correspond to the 2–5 wt % H₂O present in the melt from which the fluid originally exsolved. Higher fluid/rock ratios above 0.1 cannot form calcic–sodic brines, but result in NaCl-dominated aqueous fluids of low to moderate salinity (Fig. 14).

This simple result has two remarkable implications. First, it indicates that the entire fluid inclusion history of the Monte Matttoni mafic complex can be explained by closed-system evolution of the igneous system, starting with progressive fluid exsolution from an ascending and crystallizing magma, followed by local closed-system re-equilibration of the fluid with the solid rock down to about 200°C. Second, the results show that calcic–sodic brines, which are usually associated with evaporite-bearing sedimentary basins, can also be formed *in situ* by exsolution of only weakly saline

magmatic–hydrothermal fluids from hydrous magmas (Audétat *et al.*, 2008). Weight per cents of magmatic fluid will be expelled by any amphibole-saturated pluton in arc or orogenic settings; even the relatively volatile-poor Bushveld mafic igneous complex contains late-stage calcic–sodic brine inclusions in pegmatitic pods (Schiffries, 1990) whose formation may reflect a similar process of retrograde fluid–rock reaction. After the geologically rapid cooling of plutons, such residual magmatic brines may persist for millions of years, as the igneous body remains at ambient crustal temperatures; for example, 200°C at 6–8 km depth in the case of the Adamello batholith. Calcic–sodic brines are common in crystalline basement regions (Fritz & Frape, 1982; Leybourne & Goodfellow, 2007), and our results show that these basement brines do not necessarily require deep infiltration from overlying evaporitic basins.

Ore metal concentrations

The ore metal concentrations (Cu, Pb, Zn, W, Pb and Mn) in the different fluid inclusion types of the Monte Mattoni mafic complex can be compared with those of other mineralized and barren plutons of generally more felsic composition (Fig. 11). One of the best-studied barren intrusive complexes is the Rito del Medio pluton, a granite with miarolitic cavities hosting abundant coexisting fluid and melt inclusions in euhedral free-standing quartz crystals (Audétat *et al.*, 2008). Its fluid and melt inclusions demonstrate that a single-phase low-salinity (4.5–7.5 wt % eqv. NaCl) and low-density aqueous fluid exsolved directly from the crystallizing melt (Audétat *et al.*, 2008). In addition, compositional data for single-phase, low-salinity (2.7–13 wt % eqv. NaCl) fluid inclusions from several magmatic–hydrothermal ore deposits have been compared, including the Bajo de la Alumbrera porphyry Cu–Au–Mo deposit (Ulrich *et al.*, 2002; Audétat & Pettke, 2003; Audétat *et al.*, 2008), the Butte Cu (Mo–Ag–Zn–Au) deposit (Rusk *et al.*, 2004; Williams-Jones & Heinrich, 2005; Audétat *et al.*, 2008), and the El Teniente Cu (Mo) deposit (Klemm *et al.*, 2007; Audétat *et al.*, 2008), with supplementary S concentrations from the study of Seo *et al.* (2009).

Early magmatic–hydrothermal fluids exsolved from hornblende gabbros at Monte Mattoni (types B and C) have lower concentrations of ore-forming metals and S than unseparated input fluids generating porphyry-type ore deposits. Although the Cu concentrations of chalcopyrite-mineralized samples from the three ore deposits may be overestimated owing to post-entrapment modification (Lerchbaumer & Audétat, 2012), the fluids of Monte Mattoni contain some of the lowest Cu concentrations ever measured in high-temperature magmatic–hydrothermal fluid inclusions. It is also remarkable that all magmatic–hydrothermal fluids from the Monte Mattoni complex have rather low Fe contents (up to 3000 ppm), which contrast with the typically high Fe concentrations in ore-stage fluids of porphyry

copper deposits that can reach several weight per cent (e.g. Audétat *et al.*, 2008; Seo *et al.*, 2009). Melt inclusions in hybrid andesitic magma systems giving rise to porphyry copper mineralization show that the mafic magmas (basaltic andesite end-member) are typically more Cu-rich than the mixed and more felsic magmas (Halter *et al.*, 2005). We therefore expected that fluids exsolved from the gabbros at Monte Mattoni would be more Cu-rich than those of the felsic Rito del Medio pluton, and match more closely with the metal-rich fluids involved in economic Cu ore formation. This is not the case, suggesting that the primary magmatic–hydrothermal fluids from the mafic magmas of the Adamello batholith are inherently inefficient agents for ore mineralization.

The absence of economic ore deposits associated with this large intrusion may be due to the slow and gradual fluid release from the batholith, rather than forceful expulsion favoring ore formation (Weis *et al.*, 2012). Gradual fluid loss is indicated by the fact that only the rather small and rapidly cooled mafic intrusions of the Adamello batholith preserve any evidence of fluid saturation. The more voluminous intermediate to silicic plutons in the batholith lack any evidence of trapping pockets of exsolved fluid, even though they probably expelled much greater volumes of hydrous fluid during their crystallization.

The reason for low magma fertility regarding hydrothermal ore formation in the Adamello Batholith and the Periadriatic igneous province in general is most probably related to the melting conditions that generated the magmas in their mantle source. The absence of mantle enrichment by extended subduction-related metasomatism in the western and central segments of the Alps gave rise to the idea of pluton emplacement resulting from slab break-off, after collisional closure of a small oceanic basin (the Alpine Tethys) extending into the Alpine realm from the North Atlantic (von Blanckenburg & Davies, 1995; Handy *et al.*, 2010). This scenario of local melt generation contrasts with rich porphyry copper provinces in the Carpathian–Balkan orogen extending all the way to the Himalayas, where major subduction of oceanic lithosphere of the Neotethys created conditions for syn- and post-subduction mantle metasomatism and ore-productive calc-alkaline magmatism (Richards, 2011; Gallhofer *et al.*, 2015), comparable with the world's dominant Cu provinces associated with the long-lived magmatic arcs of the circum-Pacific region (e.g. Sillitoe, 2010).

ACKNOWLEDGEMENTS

Marcel Guillong and Jun Hung Seo are thanked for assistance during LA-ICP-MS analysis of fluid inclusions. Constructive reviews by Philip Brown, John Blundy, Stefano Salvi, Dan Marshall, Kurt Krenn, Matthew Steele-MacInnis and two anonymous reviewers helped to improve this paper.

FUNDING

Funding for this research was provided by the Swiss National Science Foundation (grant number 200020-116693).

REFERENCES

- Angus, N. S. (1962). Ocellar hybrids from the Tyrone igneous series, Ireland. *Geological Magazine* **99**, 9–26.
- Audétat, A. & Pettke, T. (2003). The magmatic–hydrothermal evolution of two barren granites: a melt- and fluid-inclusion study of the Rito del Medio und Canada Pinabete plutons in northern New Mexico (USA). *Geochimica et Cosmochimica Acta* **67**, 97–121.
- Audétat, A., Pettke, T., Heinrich, C. A. & Bodnar, R. J. (2008). The composition of magmatic–hydrothermal fluids in barren versus mineralized intrusions. *Economic Geology* **103**, 877–908.
- Bakker, R. J. (1999). Adaptation of the Bowers and Helgeson (1983) equation of state to the H_2O – CO_2 – CH_4 – N_2 – NaCl system. *Chemical Geology* **154**, 225–236.
- Bakker, R. J. (2003). Package FLUIDS 1. Computer programs for analysis of fluid inclusion data and for modeling bulk fluid properties. *Chemical Geology* **194**, 3–23.
- Bianchi, A., Callegari, E. & Jobstraibizer, P. G. (1970). I tipi Petrografici fondamentali del Plutone dell'Adamello. Tonaliti, Quarzodioriti, Granodioriti e loro Varietà leucocrate. *Memoria degli Istituti di Geologia e Mineralogia dell'Università di Padova* **27**, 1–148.
- Blundy, J. D. & Shimizu, N. (1991). Trace element evidence for plagioclase recycling in calc-alkaline magmas. *Earth and Planetary Science Letters* **102**, 178–197.
- Blundy, J. D. & Sparks, R. S. J. (1992). Petrogenesis of mafic inclusions in granitoids of the Adamello massif, Italy. *Journal of Petrology* **33**, 1039–1104.
- Bodnar, R. J. (1995). Fluid inclusion evidence for a magmatic source of metals in porphyry copper deposits. In: Thompson, J. F. H. (ed.) *Magmas, Fluids and Ore Deposits*. Mineralogical Association of Canada, Short Course Series. **23**, 139–152.
- Bodnar, R. J. & Vityk, M. O. (1994). Interpretation of microthermometric data for NaCl – H_2O fluid inclusions. In: De Vivo, B. & Frezzotti, M. L. (eds) *Fluid inclusions in minerals: Methods and applications*. Short course of the working group (IMA) *Inclusions in Minerals*. Blacksburg, VA: Virginia Polytechnic Institute and State University, pp. 117–131.
- Bowers, T. S. & Helgeson, H. C. (1983). Calculation of the thermodynamic and geochemical consequences of non-ideal mixing in the system H_2O – CO_2 – NaCl on phase relations in geological systems: equation of state for H_2O – CO_2 – NaCl fluids at high pressures and temperatures. *Geochimica et Cosmochimica Acta* **47**, 1247–1275.
- Brack, P. (1981). Structures in the southwestern border of the Adamello intrusion (Alpi Bresciane, Italy). *Schweizerische Mineralogische und Petrographische Mitteilungen* **61**, 37–50.
- Broderick, C., Wotzlaw, J. F., Frick, D. A., Gerdes, A., Ulianov, A., Günther, D. & Schaltegger, U. (2015). Linking the thermal evolution and emplacement history of an upper-crustal pluton to its lower-crustal roots using zircon geochronology and geochemistry (southern Adamello batholith, N. Italy). *Contributions to Mineralogy and Petrology* **170**, 18.
- Burnham, C. W. (1967). Hydrothermal fluids at the magmatic stage. In: Barnes, H. L. (ed.) *Geochemistry of Hydrothermal Ore Deposits*. New York: Holt, Rinehart & Winston, pp. 34–76.
- Burnham, C. W. & Ohmoto, H. (1980). Late-stage processes of felsic magmatism. *Mining Geology, Special Issue*, 1–11.
- Burrus, R. C. (1981). Analysis of phase equilibria in C–O–H–S fluid inclusions. In: Hollister, L. S. & Crawford, M. L. (eds) *Fluid Inclusions: Applications to Petrology*. Mineralogical Association of Canada, Short Course Series **6**, 39–74.
- Candela, P. (1997). Shallow, ore-related granites: Textures, volatiles and ore metals. *Journal of Petrology* **38**, 1619–1633.
- Clemens, J. D. & Watkins, J. M. (2001). The fluid regime of high-temperature metamorphism during granitoid magma genesis. *Contributions to Mineralogy and Petrology* **140**, 600–606.
- Cline, J. & Bodnar, R. J. (1991). Can economic porphyry copper mineralization be generated by a typical calc-alkaline melt? *Journal of Geophysical Research* **96**, 8113–8126.
- Coggon, R. & Holland, T. J. B. (2002). Mixing properties of phengitic micas and revised garnet–phengite thermobarometers. *Journal of Metamorphic Geology* **20**, 683–696.
- Cortecchi, G., Del Moro, A., Leone, G. & Pardini, G. C. (1979). Correlation between strontium and oxygen isotopic compositions of rocks from the Adamello Massif (Northern Italy). *Contributions to Mineralogy and Petrology* **68**, 421–427.
- Dale, J., Powell, R., White, R. W., Elmer, F. L. & Holland, T. J. B. (2005). A thermodynamic model for Ca–Na clin amphiboles in Na_2O – CaO – FeO – MgO – Al_2O_3 – SiO_2 – H_2O – O for petrological calculations. *Journal of Metamorphic Geology* **23**, 771–791.
- Del Moro, A., Ferrara, G., Tonarini, S. & Callegari, E. (1983a). Rb/Sr systematics on the rocks from the Adamello batholith (Southern Alps). *Memorie della Società Geologica Italiana* **26**, 261–284.
- Del Moro, A., Pardini, G. C., Quercioli, C., Villa, I. M. & Callegari, E. (1983b). Rb/Sr and K/Ar chronology of Adamello granitoids, southern Alps. *Memorie della Società Geologica Italiana* **26**, 285–299.
- Diamond, L. W. (1992). Stability of CO_2 clathrate hydrate + CO , liquid + CO_2 vapour + aqueous KCl – NaCl solutions: Experimental determination and application to salinity estimates of fluid inclusions. *Geochimica et Cosmochimica Acta* **56**, 273–280.
- Dolejs, D. (2007). Thermodynamic model for the simultaneous exsolution of two fluids from silicic magmas. *Geochimica et Cosmochimica Acta* **71**, A229.
- Dolejs, D. & Wagner, T. (2008). Thermodynamic modeling of non-ideal mineral–fluid equilibria in the system Si–Al–Fe–Mg–Ca–Na–K–H–O–Cl at elevated temperatures and pressures: Implications for hydrothermal mass transfer in granitic rocks. *Geochimica et Cosmochimica Acta* **72**, 526–553.
- Driesner, T. (2007). The system H_2O – NaCl . II. Correlations for molar volume, enthalpy, and isobaric heat capacity from 0 to 1000°C, 1 to 5000 bar, and 0 to 1 XNaCl. *Geochimica et Cosmochimica Acta* **71**, 4902–4919.
- Driesner, T. & Heinrich, C. A. (2007). The system H_2O – NaCl . I. Correlation formulae for phase relations in temperature–pressure–composition space from 0 to 1000°C, 0 to 5000 bar, and 0 to 1 XNaCl. *Geochimica et Cosmochimica Acta* **71**, 4880–4901.
- Eastoe, C. J. (1978). A fluid inclusion study in the Panguna porphyry copper deposit, Bougainville, Papua New Guinea. *Economic Geology* **73**, 721–748.
- Farmer, G. L. & DePaolo, D. J. (1984). Origin of Mesozoic and Tertiary granite in the western United States and implications for pre-Mesozoic crustal structure. Nd and Sr isotopic studies of unmineralized and Cu- and Mo-mineralized

- granite in the Precambrian craton. *Journal of Geophysical Research* **89**, 10141–10160.
- Floess, D. & Baumgartner, L. P. (2015). Constraining magmatic fluxes through thermal modelling of contact metamorphism. In: Caricchi, L. & Blundy, J. D. (eds) *Chemical, Physical and Temporal Evolution of Magmatic Systems. Geological Society, London, Special Publications* **422**, 41–56.
- Fritz, P. & Frape, S. K. (1982). Saline groundwaters in the Canadian shield—a first overview. *Chemical Geology* **36**, 179–190.
- Gallhofer, D., von Quadt, A., Peytcheva, I., Schmid, S. M. & Heinrich, C. A. (2015). Tectonic, magmatic, and metallogenic evolution of the Late Cretaceous arc in the Carpathian–Balkan orogen. *Tectonics* **34**, 1813–1836.
- Gerdes, M. L., Baumgartner, L. P., Person, M. & Rumble, D., III (1995). One- and two-dimensional models for fluid flow and stable isotope exchange at an outcrop in the Adamello contact aureole, Southern Alps, Italy. *American Mineralogist* **80**, 1004–1019.
- Gieré, R. (1990). Hydrothermal mobility of Ti, Zr and REE: examples from the Bergell and Adamello contact aureoles (Italy). *Terra Nova* **2**, 60–67.
- Gieré, R. & Williams, C. T. (1992). REE-bearing minerals in Ti-rich veins from the Adamello contact aureole (Italy). *Contributions to Mineralogy and Petrology* **112**, 83–100.
- Goldstein, R. H. & Reynolds, T. J. (1994). *Systematics of Fluid Inclusions in Diagenetic Materials. Society of Sedimentary Geology, Short Course Series* **31**, 199 pp.
- Guillong, M., Meier, D. L., Allan, M. M., Heinrich, C. A. & Yardley, B. W. D. (2008). SILLS: a Matlab-based program for the data reduction of laser ablation ICP-MS data of homogeneous materials and inclusions. In: Sylvester, P. (ed.) *Laser Ablation ICP-MS in the Earth Sciences: Current Practices and Outstanding Issues. Mineralogical Association of Canada, Short Course Series* **40**, 328–333.
- Günther, D., Audétat, A., Frischknecht, R. & Heinrich, C. A. (1998). Quantitative analysis of major, minor and trace elements in fluid inclusions using laser ablation-inductively coupled plasma mass spectrometry. *Journal of Analytical and Atomic Spectrometry* **13**, 263–270.
- Halter, W. E., Heinrich, C. A. & Pettker, T. (2005). Magma evolution and the formation of porphyry Cu–Au ore fluids: evidence from silicate and sulfide melt inclusions. *Mineralium Deposita* **39**, 845–863.
- Handy, M. R., Schmid, S. M., Bousquet, R., Kissling, E. & Bernoulli, D. (2010). Reconciling plate-tectonic reconstructions of Alpine Tethys with the geological–geophysical record of spreading and subduction in the Alps. *Earth-Science Reviews* **102**, 121–158.
- Hauzenberger, C. A., Baumgartner, L. P. & Pak, T. M. (2002). Experimental study on the solubility of the ‘model’-pelite assemblage albite + K-feldspar + andalusite + quartz in supercritical chloride-rich aqueous solutions at 0.2 GPa and 600°C. *Geochimica et Cosmochimica Acta* **65**, 4493–4507.
- Hedenquist, J. W. & Lowenstern, J. B. (1994). The role of magmas in the formation of hydrothermal ore deposits. *Nature* **370**, 519–527.
- Heinrich, C. A., Ryan, C. G., Mernagh, T. P. & Eadington, P. J. (1992). Segregation of ore metals between magmatic brine and vapor: a fluid inclusion study using PIXE microanalysis. *Economic Geology* **87**, 1566–1583.
- Heinrich, C. A., Pettker, T., Halter, W. E., Aigner-Torres, M., Audétat, A., Günther, D., Hattendorf, B., Bleiner, D., Guillong, M. & Horn, I. (2003). Quantitative multi-element analysis of minerals, fluid and melt inclusions by laser-ablation inductively-coupled-plasma mass spectrometry. *Geochimica et Cosmochimica Acta* **67**, 3473–3496.
- Helgeson, H. C. & Kirkham, D. H. (1976). Theoretical prediction of the thermodynamic behavior of aqueous electrolytes at high pressures and temperatures. III. Equation of state for aqueous species at infinite dilution. *American Journal of Science* **276**, 97–240.
- Helgeson, H. C., Kirkham, D. H. & Flowers, G. C. (1981). Theoretical prediction of the thermodynamic behavior of aqueous electrolytes at high pressures and temperatures. IV. Calculation of activity coefficients, osmotic coefficients, and apparent molal and standard and relative partial molal properties to 600°C and 5 KB. *American Journal of Science* **281**, 1249–1516.
- Hendry, D. A. F., Chivas, A. R., Long, J. V. P. & Reed, S. J. B. (1985). Chemical differences between minerals from mineralizing and barren intrusions from some North American porphyry copper deposits. *Contributions to Mineralogy and Petrology* **89**, 317–329.
- Holland, T. & Powell, R. (1996). Thermodynamics of order–disorder in minerals. II. Symmetric formalism applied to solid solutions. *American Mineralogist* **81**, 1425–1437.
- Holland, T. J. B. & Powell, R. (1998). An internally consistent thermodynamic data set for phases of petrological interest. *Journal of Metamorphic Geology* **16**, 309–343.
- Holland, T. & Powell, R. (2003). Activity–composition relations for phases in petrological calculations: an asymmetric multi-component formulation. *Contributions to Mineralogy and Petrology* **145**, 492–501.
- Holland, T., Baker, J. & Powell, R. (1998). Mixing properties and activity–composition relationships of chlorites in the system MgO–FeO–Al₂O₃–SiO₂–H₂O. *European Journal of Mineralogy* **10**, 395–406.
- Hollister, L. S. & Burrus, R. C. (1976). Phase equilibria in fluid inclusions from the Khtada Lake metamorphic complex. *Geochimica et Cosmochimica Acta* **40**, 163–175.
- Holloway, J. R. & Blank, J. G. (1994). Application of experimental results to C–O–H species in natural melts. In: Carroll, M. R. & Holloway, J. R. (eds) *Volatiles in Magmas. Mineralogical Society of America, Reviews in Mineralogy* **30**, 187–230.
- Holtz, F., Behrens, H., Dingwell, D. B. & Johannes, W. (1995). Water solubility in haplogranitic melts. Compositional, pressure and temperature dependence. *American Mineralogist* **80**, 95–108.
- Holtz, F., Johannes, W., Tamic, N. & Behrens, H. (2001). Maximum and minimum water contents of granitic melts generated in the crust: a reevaluation and implications. *Lithos* **56**, 1–14.
- Hsu, Y. J. (2016). Solid–melt–liquid–vapor equilibria in crustal magmatic and hydrothermal systems: An experimental study. PhD thesis No. 23851, ETH Zurich, 150 pp.
- Johnson, J. W., Oelkers, E. H. & Helgeson, H. C. (1992). SUPCRT92: a software package for calculating the standard molal thermodynamic properties of minerals, gases, aqueous species, and reactions from 1 to 5000 bars and 0 to 1000°C. *Computers and Geosciences* **18**, 899–947.
- Karpov, I. K., Chudnenko, K. V. & Kulik, D. A. (1997). Modeling chemical mass transfer in geochemical processes: Thermodynamic relations, conditions of equilibria, and numerical algorithms. *American Journal of Science* **297**, 767–806.
- Kesler, S. E. & Simon, A. C. (2015). *Mineral Resources, Economics and the Environment*, 2nd edn. Cambridge: Cambridge University Press, 446 pp.
- Kesler, S. E., Issigoni, M. J., Brownlow, A. H., Damon, P. E., Moore, W. J., Northcote, K. E. & Preto, V. A. (1975). Geochemistry of biotite from mineralized and barren intrusive systems. *Economic Geology* **70**, 559–567.

- Kestin, J., Sengers, J. V., Kamgar-Parsi, B. & Levelt-Sengers, J. M. (1984). Thermophysical properties of fluid H₂O. *Journal of Physical and Chemical Reference Data* **13**, 175–183.
- Kilinc, I. A. & Burnham, W. C. (1972). Partitioning of chloride between a silicate melt and coexisting aqueous phase from 2 to 8 kilobars. *Economic Geology* **67**, 231–235.
- Klemm, L. M., Pettke, T. & Heinrich, C. A. (2007). Hydrothermal evolution of the El Teniente deposit, Chile: Porphyry Cu–Mo ore deposition from low-salinity magmatic fluids. *Economic Geology* **102**, 1021–1045.
- Kulik, D. A., Wagner, T., Dmytrieva, S., Kosakowski, G., Hingerl, F. F., Chudnenko, K. & Berner, U. R. (2013). GEM-Selektor geochemical modeling package: Revised algorithm and GEMS3K numerical kernel for coupled simulation codes. *Computational Geosciences* **17**, 1–24.
- Lang, J. R. & Titley, S. R. (1998). Isotopic and geochemical characteristics of Laramide magmatic systems in Arizona and implications for the genesis of porphyry copper deposits. *Economic Geology* **93**, 138–170.
- Laubscher, H. P. (1983). The late Alpine (Periadriatic) intrusions and the Insubric Line. *Memorie della Società Geologica Italiana* **26**, 21–30.
- Lerchbaumer, L. & Audétat, A. (2012). High Cu concentrations in vapor-type fluid inclusions: An artifact? *Geochimica et Cosmochimica Acta* **88**, 255–274.
- Leybourne, M. I. & Goodfellow, W. D. (2007). Br/Cl ratios and O, H, C, and B isotopic constraints on the origin of saline waters from eastern Canada. *Geochimica et Cosmochimica Acta* **71**, 2209–2223.
- Liebscher, A. & Heinrich, C. A. (eds) (2007). *Fluid–Fluid Interactions. Mineralogical Society of America and Geochemical Society, Reviews in Mineralogy and Geochemistry* **65**, 430 pp.
- London, D. (2005). Granitic pegmatites: an assessment of current concepts and directions for the future. *Lithos* **80**, 281–303.
- London, D. (2009). The origin of primary textures in granitic pegmatites. *Canadian Mineralogist* **47**, 697–724.
- Longerich, H. P., Jackson, S. E. & Günther, D. (1996). Laser ablation inductively coupled plasma mass spectrometry transient signal data acquisition and analyte concentration calculation. *Journal of Analytical Atomic Spectrometry* **11**, 899–904.
- Lu, Y. J., Loucks, R. R., Fiorentini, M. L., Yang, Z.-M. & Hou, Z. Q. (2015). Fluid flux melting generated postcollisional high Sr/Y copper ore-forming water-rich magmas in Tibet. *Geology* **43**, 583–586.
- Macera, P., Ferrara, G., Pescia, A. & Callegari, E. (1983). A geochemical study on the acid and basic rocks of the Adamello batholith. *Memorie della Società Geologica Italiana* **26**, 223–259.
- Mason, D. R. & Feiss, P. G. (1979). On the relationship between whole rock chemistry and porphyry copper mineralization. *Economic Geology* **74**, 1506–1510.
- Oakes, C. S., Bodnar, R. J. & Simonson, J. M. (1990). The system NaCl–CaCl₂–H₂O. 1. The ice liquidus at 1 atm total pressure. *Geochimica et Cosmochimica Acta* **54**, 19–41.
- Pak, T. M., Hauenberger, C. A. & Baumgartner, L. P. (2003). Solubility of the assemblage albite + K-feldspar + andalusite + quartz in supercritical aqueous chloride solutions at 650°C and 2 kbar. *Chemical Geology* **200**, 377–393.
- Papale, P., Moretti, R. & Barbato, D. (2006). The compositional dependence of the saturation surface of H₂O + CO₂ fluids in silicate melts. *Chemical Geology* **229**, 78–95.
- Pitzer, K. S. (1995). *Thermodynamics*, 3rd edn. New York: McGraw–Hill, 626 pp.
- Powell, R. & Holland, T. (1993). On the formulation of simple mixing models for complex phases. *American Mineralogist* **78**, 1174–1180.
- Powell, R. & Holland, T. (1999). Relating formulations of the thermodynamics of mineral solid solutions: Activity modeling of pyroxenes, amphiboles, and micas. *American Mineralogist* **84**, 1–14.
- Reynolds, T. J. & Beane, R. E. (1985). Evolution of hydrothermal fluid characteristics in the Santa Rita, New Mexico, porphyry copper deposit. *Economic Geology* **80**, 1328–1374.
- Richards, J. P. (2011). Magmatic to hydrothermal metal fluxes in convergent and collided margins. *Ore Geology Reviews* **40**, 1–26.
- Roedder, E. (1971). Fluid inclusion studies on the porphyry type ore deposits at Bingham, Utah, Butte, Montana and Climax, Colorado. *Economic Geology* **66**, 98–120.
- Rohrlach, B. D. & Loucks, R. R. (2005). Multi-million-year cyclic ramp-up of volatiles in a lower-crustal magma reservoir trapped below the Tampakan copper–gold deposit by Mio-Pliocene crustal compression in the southern Philippines. In: Porter, T. M. (ed.) *Super Porphyry Copper and Gold Deposits: A Global Perspective*. Adelaide, SA: PGC, pp. 1–43.
- Rusk, B. G., Reed, M. H., Dilles, J. H., Klemm, L. M. & Heinrich, C. A. (2004). Compositions of magmatic–hydrothermal fluids determined by LA-ICPMS of fluid inclusions from the porphyry copper–molybdenum deposit at Butte, MT. *Chemical Geology* **210**, 173–199.
- Schaltegger, U., Brack, P., Ovtcharova, M., Peytcheva, I., Schoene, B., Stracke, A., Marocchi, M. & Bargossi, G. M. (2009). Zircon and titanite recording 1.5 million years of magma accretion, crystallization and initial cooling in a composite pluton (southern Adamello batholith, northern Italy). *Earth and Planetary Science Letters* **286**, 208–218.
- Schiffries, C. M. (1990). Liquid-absent aqueous fluid inclusions and phase equilibria in the system CaCl₂–NaCl–H₂O. *Geochimica et Cosmochimica Acta* **54**, 611–619.
- Schoene, B., Schaltegger, U., Brack, P., Latkoczy, C., Stracke, A. & Günther, D. (2012). Rates of magma differentiation and emplacement in a ballooning pluton recorded by U–Pb TIMS–TEA, Adamello batholith, Italy. *Earth and Planetary Science Letters* **355**, 162–173.
- Seo, J. H., Guillong, M. & Heinrich, C. A. (2009). The role of sulfur in the formation of magmatic–hydrothermal copper–gold deposits. *Earth and Planetary Science Letters* **282**, 323–328.
- Sharygin, A. V., Wood, R. H., Zimmerman, G. H. & Balashov, V. N. (2002). Multiple ion association versus redissociation in aqueous NaCl and KCl at high temperatures. *Journal of Physical Chemistry B* **106**, 7121–7134.
- Shinohara, H. (1994). Exsolution of immiscible vapor and liquid phases from crystallizing silicate melt: implications for chlorine and metal transport. *Geochimica et Cosmochimica Acta* **58**, 5215–5221.
- Shock, E. L. & Helgeson, H. C. (1988). Calculation of the thermodynamic and transport properties of aqueous species at high pressures and temperatures: Correlation algorithms for ionic species and equation of state predictions to 5 kb and 1000°C. *Geochimica et Cosmochimica Acta* **52**, 2009–2036.
- Shock, E. L., Helgeson, H. C. & Sverjensky, D. A. (1989). Calculation of the thermodynamic and transport properties of aqueous species at high pressures and temperatures: Standard partial molal properties of inorganic neutral species. *Geochimica et Cosmochimica Acta* **53**, 2157–2183.
- Shock, E. L., Sassani, D. C., Willis, M. & Sverjensky, D. A. (1997). Inorganic species in geological fluids: Correlations among

- standard molal thermodynamic properties of aqueous ions and hydroxide complexes. *Geochimica et Cosmochimica Acta* **61**, 907–950.
- Sillitoe, R. H. (2010). Porphyry copper systems. *Economic Geology* **105**, 3–41.
- Sonderegger, U. C. (1980). Geologie und Petrographie des südlichen Adamello: IV Monte Mattoni. Diploma thesis, ETH Zürich, 102 pp.
- Sverjensky, D. A., Shock, E. L. & Helgeson, H. C. (1997). Prediction of the thermodynamic properties of aqueous metal complexes to 1000°C and 5 kb. *Geochimica et Cosmochimica Acta* **61**, 1359–1412.
- Tagirov, B. & Schott, J. (2001). Aluminum speciation in crustal fluids revisited. *Geochimica et Cosmochimica Acta* **65**, 3965–3992.
- Tagirov, B., Zotov, A. V. & Akinfiev, N. N. (1997). Experimental study of dissociation of HCl from 350 to 500°C and from 500 to 2500 bars. Thermodynamic properties of HClO(aq). *Geochimica et Cosmochimica Acta* **61**, 4267–4280.
- Tanger, J. C. & Helgeson, H. C. (1988). Calculation of the thermodynamic and transport properties of aqueous species at high pressures and temperatures: Revised equations of state for the standard partial molal properties of ions and electrolytes. *American Journal of Science* **288**, 19–98.
- Thiery, R., van den Kerkhof, A. M. & Dubessy, J. (1994). vX properties of CH₄–CO₂ and CO₂–N₂ fluid inclusions; modelling for $T < 31^\circ\text{C}$ and $P < 400$ bars. *European Journal of Mineralogy* **6**, 753–771.
- Touret, J. (1982). An empirical phase diagram for a part of the N₂–CO₂ system at low temperatures. *Chemical Geology* **37**, 49–58.
- Ulmer, P., Callegari, E. & Sonderegger, U. C. (1985). Genesis of the mafic and ultramafic rocks and their genetical relations to the tonalitic–trondjemitic granitoids of the southern Adamello batholith, northern Italy. *Memorie della Società Geologica Italiana* **26**, 171–222.
- Ulmer, P. (1986). Basische und ultrabasische Gesteine des Adamello (Provinzen Brescia und Trento, Norditalien). PhD thesis, ETH Zürich, Dissertation 8105, 274 pp.
- Ulrich, T., Günther, D. & Heinrich, C. A. (2002). The evolution of a porphyry Cu–Au deposit, based on LA-ICPMS analysis of fluid inclusions: Bajo de la Alumbrera, Argentina. *Economic Geology* **97**, 1889–1920.
- von Blanckenburg, F. & Davies, J. H. (1995). Slab breakoff—a model for syn-collisional magmatism and tectonics in the Alps. *Tectonics* **14**, 120–131.
- Wagner, T., Kulik, D. A., Hingerl, F. F. & Dmytrieva, S. (2012). GEM-Selektor geochemical modeling package: TSolMod library and data interface for multicomponent phase models. *Canadian Mineralogist* **50**, 1173–1195.
- Walther, J. V. (1997). Determination of activity coefficients of neutral species in supercritical H₂O solutions. *Geochimica et Cosmochimica Acta* **61**, 3311–3318.
- Walther, J. V. (2001). Experimental determination and analysis of the solubility of corundum in 0.1 and 0.5M NaCl solutions between 400 and 600°C from 0.5 to 2.0 kbar. *Geochimica et Cosmochimica Acta* **65**, 2843–2851.
- Warren, C. J. & Waters, D. J. (2006). Oxidized eclogites and garnet–blueschists from Oman: P – T path modelling in the NCFMASHO system. *Journal of Metamorphic Geology* **24**, 783–802.
- Webster, J. D. (2004). The exsolution of magmatic hydrosaline chloride liquids. *Chemical Geology* **210**, 33–48.
- Wei, C. J., Powell, R. & Zhang, L. F. (2003). Eclogites from the south Tianshan, NW China: petrological characteristics and calculated mineral equilibria in the Na₂O–CaO–FeO–MgO–Al₂O₃–SiO₂–H₂O system. *Journal of Metamorphic Geology* **21**, 163–179.
- Weis, P., Driesner, T. & Heinrich, C. A. (2012). Porphyry-copper ore shells form at stable pressure–temperature fronts within dynamic fluid plumes. *Science* **338**, 1613–1616.
- Williams-Jones, A. E. & Heinrich, C. A. (2005). Vapor transport of metals and the formation of magmatic–hydrothermal ore deposits. *Economic Geology* **100**, 1287–1312.
- Zhang, Y. & Frantz, J. D. (1987). Determination of homogenization temperature and densities of supercritical fluid in the system NaCl–KCl–CaCl₂–H₂O using synthetic fluid inclusions. *Chemical Geology* **64**, 335–350.

APPENDIX: CALCULATION SCHEME FOR FLUID INCLUSION COMPOSITIONS

Absolute solute concentrations (in ppm) were calculated by combining the apparent salinity (obtained from microthermometry) and element ratios determined by LA-ICP-MS (Heinrich *et al.*, 1992; Guillon *et al.*, 2008). The following mass-balance equations relate absolute element concentrations to apparent salinity:

$$m_{\text{S}^*} = m_{\text{NaCl}} + 0.5 \sum \frac{(\text{ppm}_{\text{Me}}) \frac{M_{\text{MeCl}_n}}{M_{\text{Me}}}}{10^4} \quad (\text{A1})$$

$$m_{\text{S}^*} = m_{\text{NaCl}} + 0.5 \sum m_{\text{MeCl}_n} \quad (\text{A2})$$

Here m_{S^*} is the mass of NaCl eqv. in 100 g fluid (apparent salinity), m_{NaCl} is the mass of NaCl, and m_{MeCl_n} is the mass of any other metal chloride (e.g. KCl, CaCl₂, MgCl₂, FeCl₂). M_{MeCl_n} and M_{Me} are the molar masses of metal chloride and metal, respectively. Conversion of element concentration data into solute molalities (mol kg^{−1} H₂O) is straightforward for aqueous H₂O–NaCl fluids, and can be done with the following equations:

$$m_{\text{S}} = \sum m_{\text{Me}} + m_{\text{Cl}} \quad (\text{A3})$$

$$m_{\text{Cl}} = \left(\sum n_{\text{Me},z+} + 2 \sum n_{\text{Me},z2+} \right) M_{\text{Cl}} \quad (\text{A4})$$

$$m_{\text{H}_2\text{O}} = 100 - m_{\text{S}} \quad (\text{A5})$$

where m_{S} is the mass of salt in 100 g fluid (true salinity), and m_{Me} , m_{Cl} and $m_{\text{H}_2\text{O}}$ are the masses of metals, Cl and H₂O. The mole numbers of monovalent and divalent cations are denoted by $n_{\text{Me},z+}$ and $n_{\text{Me},z2+}$, and M_{Cl} is the molar mass of Cl.

Calculations for H₂O–NaCl–CO₂ fluids require solving a system of linear equations that is obtained from the following expressions:

$$R_{\text{S}} = \frac{m_{\text{S}}}{m_{\text{S}} + m_{\text{H}_2\text{O}}} \quad (\text{A6})$$

$$R_{\text{CO}_2} = \frac{m_{\text{CO}_2}}{m_{\text{CO}_2} + m_{\text{H}_2\text{O}}} \quad (\text{A7})$$

$$m_S + m_{H_2O} + m_{CO_2} = 100. \quad (A8)$$

The ratios R_{CO_2} (fraction of CO_2) and R_S (salinity in the aqueous phase) are obtained from the microthermometric data. Solving for the masses of salt, H_2O and CO_2 results in

$$m_S = \frac{100R_S(R_{CO_2} - 1)}{R_{CO_2}R_S - 1} \quad (A9)$$

$$m_{H_2O} = -\frac{100(R_{CO_2} - 1)(R_S - 1)}{R_{CO_2}R_S - 1} \quad (A10)$$

$$m_{CO_2} = \frac{100R_{CO_2}(R_S - 1)}{R_{CO_2}R_S - 1}. \quad (A11)$$

The molalities of all dissolved solutes can be calculated from m_S , m_{H_2O} , m_{CO_2} and equations (A3) and (A4).